

METHODS FOR OPTIMIZATION OF A LAUNCH VEHICLE FOR PRESSURE
FLUCTUATION LEVELS AND AXIAL FORCE

Except where reference is made to the work of others, the work described in this thesis is my own or was done in collaboration with my advisory committee. This thesis does not include proprietary or classified information.

Scott Walter Thomas

Certificate of Approval:

Brian Thurow
Assistant Professor
Aerospace Engineering

Roy J. Hartfield, Chair
Professor
Aerospace Engineering

Robert Gross
Associate Professor
Aerospace Engineering

George T. Flowers
Interim Dean
Graduate School

METHODS FOR OPTIMIZATION OF A LAUNCH VEHICLE FOR PRESSURE
FLUCTUATION LEVELS AND AXIAL FORCE

Scott Walter Thomas

A Thesis

Submitted to

the Graduate Faculty of

Auburn University

in Partial Fulfillment of the

Requirements for the

Degree of

Master of Science

Auburn, Alabama
August 9, 2008

METHODS FOR OPTIMIZATION OF A LAUNCH VEHICLE FOR PRESSURE
FLUCTUATION LEVELS AND AXIAL FORCE

Scott Walter Thomas

Permission is granted to Auburn University to make copies of this thesis at its discretion, upon request of the individuals or institutions and at their expense. The author reserves all publication rights.

Signature of Author

Date of Graduation

VITA

Scott Walter Thomas was born on February 24, 1982, in Huntsville, Alabama to James Thomas and Violet Rigdon. He grew up in a small town south of Huntsville called Lacey's Spring and went to high school at A. P. Brewer High School. Upon graduating high school he started college at Wallace State Community College in August 2000 then transferred to Calhoun Community College the next semester in January 2001. He later transferred to Auburn University in August 2002 where he pursued an Aerospace Engineering degree. As an undergraduate student he became a member of several honor societies and also worked alternating semesters as a co-op engineer with Aerotron AirPower, Inc. in LaGrange, GA through the Auburn University Co-op program. Scott graduated Magna Cum Laude with a Bachelor of Aerospace Engineering degree in May 2006. He went on to attend graduate school at Auburn University pursuing a Master's of Science in Aerospace Engineering.

THESIS ABSTRACT

METHODS FOR OPTIMIZATION OF A LAUNCH VEHICLE FOR PRESSURE
FLUCTUATION LEVELS AND AXIAL FORCE

Scott Walter Thomas

Master of Science, August 9, 2008
(B.A.E., Auburn University, 2006)

83 Typed Pages

Directed by Roy J. Hartfield, Jr.

A computational fluid dynamics (CFD) code has been combined with a Genetic Algorithm (GA) to perform a shape optimization study on a two dimensional axisymmetric model of a typical launch vehicle. The objective of this study was to demonstrate a methodology for reducing pressure fluctuations and the axial force coefficient for a launch vehicle throughout a typical ascent trajectory. Due to the high computational expense and difficulty of generating an adequate mesh autonomously, few CFD driven GA optimizations have been conducted. Some of the complexity of this process was alleviated by using a simple two dimensional axisymmetric geometry to model the vehicle.

The optimization process involved the GA selecting a set of geometric parameters that define the shape of the vehicle. A grid generator created a mesh based on these

parameters and a CFD solver calculated the flow parameters. The grid generator is a FORTRAN routine written for this particular geometric shape. The FORTRAN code created a mesh file dependent only on the geometric variables chosen by the GA. The pressure fluctuation level and axial force coefficient are calculated by the flow parameters that are obtained from the CFD solution.

A pressure fluctuation level minimization study and axial force minimization study were conducted separately using the same CFD model. The results of each optimization study were compared to a baseline geometry having a very similar shape to the Ares I Crew Launch Vehicle. The results of the pressure fluctuation study yielded a reduction in the average RMS pressure fluctuation level throughout the ascent trajectory. The average RMS fluctuating pressure level was reduced by approximately 17.5% compared to the baseline geometry; however the optimized geometry would not be favorable as a practical design for a launch vehicle shape. While the resulting optimized geometry for the pressure fluctuation study is not an ideal design, the methodology for reducing pressure fluctuations using a GA combined with CFD is shown. The axial force minimization study yielded a reduction in the axial force coefficient of approximately 56%. The resulting shape from the axial force minimized solution was found to resemble that of a blunted ogive, as expected.

ACKNOWLEDGEMENTS

The author would like to thank Dr. Roy Hartfield for his guidance and patience with this thesis as well as Ravi Duggirala and Josh Doyle for their assistance regarding technical matters involving the Linux cluster and CFD solver. The author also wishes to thank the author of the IMPROVE 3.1 Genetic Algorithm, Dr. Murray Anderson. The author would also like to thank his friends, family, and fiancé for their ongoing support and motivation as he worked to complete this thesis.

Style manual or journal used:

The American Institute of Aeronautics and Astronautics Journal

Computer software used:

Improve 3.1 Genetic Algorithm, Fluent, Tecplot 360, Force 2.0 Fortran Compiler,

Microsoft Excel, Microsoft Word

TABLE OF CONTENTS

LIST OF FIGURES.....	x
LIST OF TABLES	xiii
NOMENCLATURE.....	xiv
1 INTRODUCTION	1
2 LAUNCH VEHICLE MODEL.....	4
2.1 MODEL GEOMETRY.....	4
2.2 FLIGHT CONDITIONS	6
2.3 CFD MODEL	8
2.4 MESHING THE MODEL.....	9
2.5 GRID REFINEMENT STUDY.....	12
2.6 PRESSURE FLUCTUATION MODEL	19
3 LAUNCH VEHICLE OPTIMIZATION	22
3.1 CODE STRUCTURE.....	22
3.2 PRESSURE FLUCTUATION MINIMIZATION STUDY	26
3.2.1 CONVERGENCE CRITERIA	26
3.2.2 PRESSURE FLUCTUATION MINIMIZATION RESULTS.....	29
3.3 AXIAL FORCE MINIMIZATION STUDY.....	44
3.3.1 CONVERGENCE CRITERIA	44
3.3.2 AXIAL FORCE MINIMIZATION RESULTS.....	47
4 CONCLUSIONS AND RECOMMENDATIONS	61
REFERENCES.....	65
APPENDIX A: GA Input File.....	69

LIST OF FIGURES

Figure 1: 3D Representation of Launch Vehicle Geometry.....	4
Figure 2: Launch Vehicle Geometry with Design Variables	6
Figure 3: Altitude and Dynamic Pressure as a Function of Mach Number	7
Figure 4: Example of Launch Vehicle Mesh	10
Figure 5: Close-up of Grid Near Conic Sections	11
Figure 6: Comparison of Course and Fine Mesh	13
Figure 7: Axial Force Convergence for Considered Meshes in Refinement Study	14
Figure 8: Axial Force Coefficient Throughout Ascent for Course and Fine Mesh.....	16
Figure 9: Comparison of Computation Times at Each Flight Condition	17
Figure 10: Pressure Distribution Plot for Course Grid.....	18
Figure 11: Pressure Distribution Plot for Fine Grid.....	18
Figure 12: Location of Pressure Fluctuation Level Calculation	19
Figure 13: Effect of Flight Speed on Velocity Profiles.....	20
Figure 14: Flow Diagram for a Typical Genetic Algorithm	23
Figure 15: Flow Diagram for GA Running Multiple Members Simultaneously	24
Figure 16: Residuals and Local Pressure Convergence for the Course Mesh and Mach 0.85 Flight Condition	28
Figure 17: Fluctuating Pressure Level throughout Ascent for Baseline and Optimized Geometries	31
Figure 18: Maximum Average and Minimum Pressure Fluctuation Level Evolution.....	32

Figure 19: Minimum Fluctuating Pressure Level Evolution.....	33
Figure 20: Pressure Fluctuation Level Study Geometry Comparison.....	34
Figure 21: Pressure Fluctuation Study Variable Distribution for Rc1	36
Figure 22: Pressure Fluctuation Study Variable Distribution for Rc2	37
Figure 23: Pressure Fluctuation Study Variable Distribution for LcTot.....	38
Figure 24: Pressure Fluctuation Study Variable Distribution for Lc1	39
Figure 25: Pressure Fluctuation Study Variable Distribution for Lc3	40
Figure 26: Pressure Fluctuation Study Pressure Distribution Plot for Baseline and Optimized Geometries for Mach 0.85 Flight Condition	41
Figure 27: Pressure Fluctuation Study Dynamic Pressure Distribution Plot for Baseline and Optimized Geometries for Mach 1.50 Flight Condition	42
Figure 28: Pressure Fluctuation Study Velocity Distribution Plot Comparison at Mach 0.85 Flight Condition	43
Figure 29: Velocity Distribution Close-Up for Baseline and Optimized Geometries for Pressure Fluctuation Study at Mach 0.85.....	44
Figure 30: Residuals and Axial Force Coefficient Convergence for the Course Mesh and Mach 0.85 Flight Condition	46
Figure 31: Axial Force Coefficient throughout Ascent for Baseline and Optimized Geometries	48
Figure 32: Maximum Average and Minimum Axial Force Coefficient Evolution	49
Figure 33: Minimum Axial Force Coefficient Evolution	50
Figure 34: Best Performer and Baseline Geometry Comparison.....	52
Figure 35: Axial Force Study Variable Distribution for Rc1	53

Figure 36: Axial Force Study Variable Distribution for Rc2.....	54
Figure 37: Axial Force Study Variable Distribution for LcTot	55
Figure 38: Axial Force Study Variable Distribution for Lc1	56
Figure 39: Axial Force Study Variable Distribution for Lc3	57
Figure 40: Axial Force Study Pressure Distribution for Baseline and Optimized Geometries at Mach 1.50 Flight Condition.....	59

LIST OF TABLES

Table 1: Geometric Parameters and Dimensions of Baseline Launch Vehicle.....	6
Table 2: Flight Conditions Considered During the Ascent Trajectory	8
Table 3: Mesh Sizes Considered for Grid Refinement Study	13
Table 4: Prescribed Design Space for Both Optimization Studies.....	26
Table 5: Optimized Parameters and Design Space	51

NOMENCLATURE

CFD	-	Computational Fluid Dynamics
GA	-	Genetic Algorithm
$Rc1$	-	Radius of 1 st Conic Section
$Rc2$	-	Radius of 2 nd Conic Section
$LcTot$	-	Total Length of Conic Sections
$Lc1$	-	Length of 1 st Conic Section
$Lc2$	-	Length of 2 nd Conic Section
RANS	-	Reynolds Averaged Navier Stokes
LES	-	Large Eddy Simulation
k	-	Turbulent Kinetic Energy
ε	-	Turbulent Dissipation Rate
RNG	-	Renormalization Group
i	-	Grid Direction Parallel to Wall
j	-	Grid Direction Perpendicular to Wall
y^+	-	Normalized Turbulence Length

1 INTRODUCTION

Pressure fluctuation levels have long been a concern among launch vehicle and aircraft designers.¹⁻⁴ These pressure fluctuations are the result of turbulent flow passing over the surface of the vehicle and are often referred to as aerodynamic noise. The pressure fluctuations can be severe for certain high Reynolds number, high dynamic pressure flows, and the fluctuations can be translated to the structure of the vehicle as vibration which is of great significance concerning structural integrity. The resulting vibration can lead to fatigue and potentially severe damage to the vehicle or sensitive equipment during flight. Pressure fluctuations are predominately important during the ascent phase of the launch vehicle and are particularly important during the transonic flight regime and near the maximum dynamic pressure point in the flight. The most severe cases occur when transonic conditions overlay with maximum dynamic pressure conditions. An additional interest during the ascent phase of launch vehicles and for missiles is axial force reduction. This thesis presents a methodology for accomplishing both pressure fluctuation reduction and axial force reduction.

Adjoint methods⁵ and other gradient based approaches⁶ have been demonstrated to be effective for well-behaved aerodynamic shape optimization applications. For less well-behaved problems and for problems with discrete design variables or problems with discontinuous objective functions, population based techniques offer a more versatile and

robust approach to optimization, especially if multiple design goals are considered. In particular, binary encoded Genetic Algorithms have been shown to be effective and robust for a range of complex aerodynamic design optimization applications.⁷⁻⁴⁰ For robustness in dealing with a range of potential objective functions involving the prediction of pressure fluctuation levels, the Genetic Algorithm based approach was chosen for this effort.

Applications of Genetic Algorithms (GA's) in the aerospace industry include design of wings, airfoils and propellers,⁷⁻¹⁷ missiles and rockets,¹⁸⁻²⁵ structures,²⁶ flight and orbital trajectories,^{27,28} and control systems.²⁹⁻³¹ This thesis describes the use of a GA to optimize the aerodynamic shape for the forebody of a launch vehicle. The GA used for this study is the IMPROVE© code written by Dr. Murray Anderson.³² This is a binary encoded tournament based GA and features many advanced techniques such as a pareto option, nicheing, and elitism and is used in Refs. 17, 19-23, 35, 39, and 40. The population members for this study are similar geometric shapes which are initially randomly produced by the GA within a prescribed design space. Once a geometric shape is defined the GA passes the member to an objective function where a grid for the geometry is generated and the flow parameters are calculated by a computational fluid dynamics (CFD) solver. The value of the parameter to be minimized is then sent back to the GA for evaluation of that member's performance. The goal of the GA is to find a geometric shape with minimum pressure fluctuation level or axial force coefficient throughout several flight conditions in a typical launch trajectory.

The objective function for this effort is a combination of aerodynamic parameters obtained from CFD solutions for the flow surrounding candidate designs. The use of a

CFD model as an objective function for a GA can be very computationally expensive. In order to shorten run times the CFD solver is run on a Linux cluster of microprocessors. Also a simple two-dimensional axisymmetric model is employed to further reduce the computational demands. Various configurations were tested to determine which solver model to use as well as what grid size to use for the model. This paper describes the development of the CFD model and the implementation of this model into the GA to minimize the fluctuating pressure level and axial force coefficient. The procedure for combining a CFD solver with a GA is similar to that described in Refs. 35, 39 and 40 for freight truck applications.

2 LAUNCH VEHICLE MODEL

2.1 MODEL GEOMETRY

The geometric shape that is of interest for this study is the forebody of a launch vehicle. The particular vehicle shape used in this study is based on the proposed geometry for the Ares I Crew Exploration Vehicle. To clearly show the vehicle shape a three dimensional representation of the geometry is shown in Figure 1. The geometry consists of a blunted ogive nose tip followed by a slender cylindrical section. The geometry then expands through three conic sections to a larger cylindrical section.

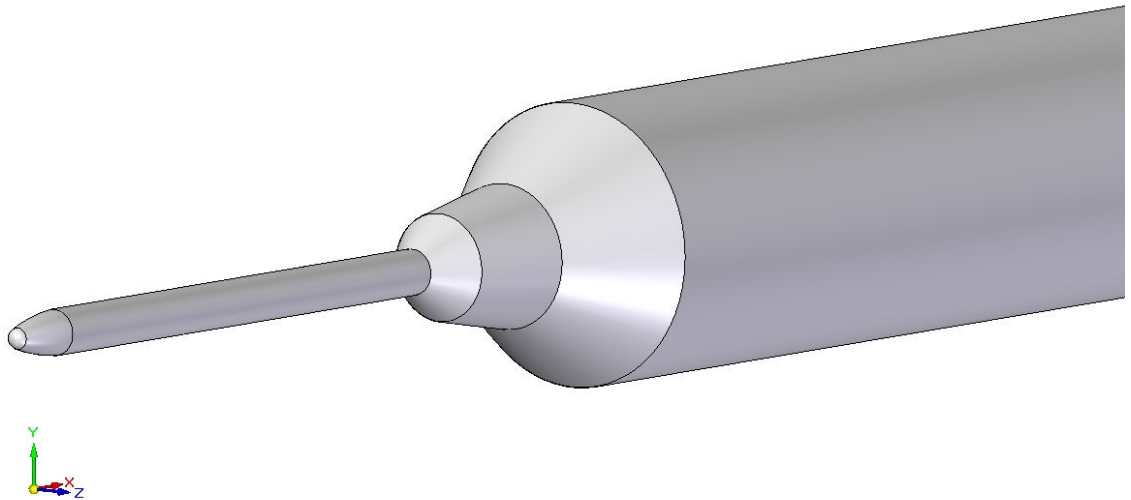


Figure 1: 3D Representation of Launch Vehicle Geometry

The 2D axisymmetric model used in this study and the variables defining the geometry are shown in Figure 2. This geometry is axisymmetric about the dotted line.

Note that the length of the model shown in Figure 2 is shortened to more clearly show the geometry features. The geometry is completely defined by the eleven variables shown in Figure 2, however not all variables are included as design variables. For this study the only dimensions changed during the GA optimization process are the dimensions defining the three conic sections. These variables are $Rc1$, $Rc2$, $LcTot$, $Lc1$, and $Lc3$ as shown in Figure 2. The remaining dimensions are held constant but are included in the model to more accurately capture the flow characteristics. Also, the aft end of the launch vehicle is not included in the model since only the forebody of the vehicle is of interest in this study. The actual parameters adjusted by the GA are dimensionless parameters where the cone radii and total length of the conic sections are relative to the base diameter, Rb , and the length of each conic section is relative to the total length of the conic sections. The dimensionless parameters that define the baseline model for this study are shown in Table 1. This baseline geometry was chosen to resemble the Ares I Crew Launch Vehicle.

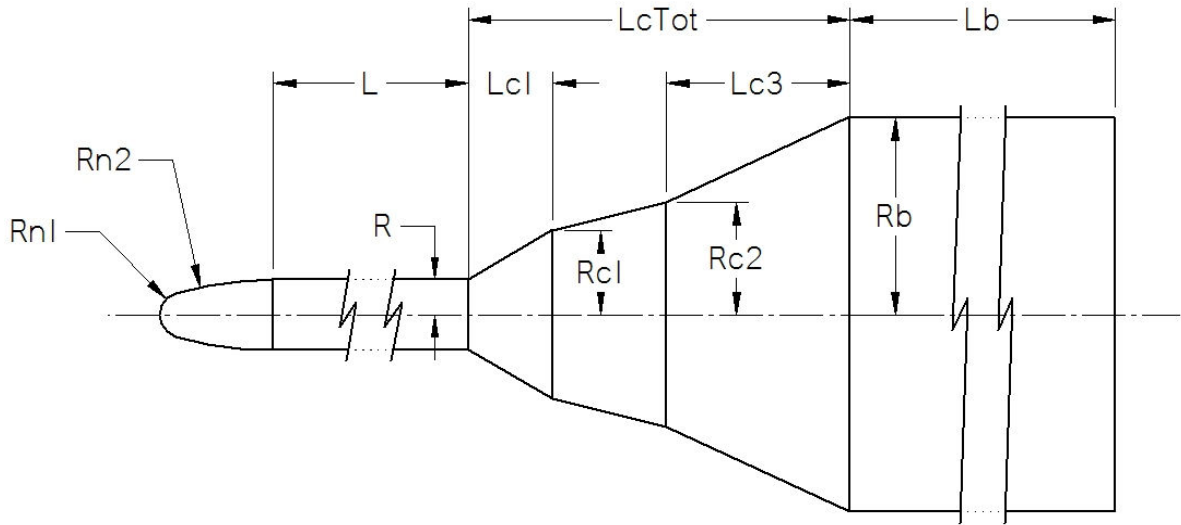


Figure 2: Launch Vehicle Geometry with Design Variables

Table 1: Geometric Parameters and Dimensions of Baseline Launch Vehicle

<i>Parameter</i>	<i>Dimensionless</i>	<i>In meters</i>
Rb	1.00	2.5380
Rc1	0.75	0.9518
Rc2	0.50	1.2690
LcTot	2.00	5.0760
Lc1	0.15	0.7614
Lc3	0.45	2.2842

2.2 FLIGHT CONDITIONS

The goal of this study is to demonstrate a methodology for optimizing a launch vehicle shape with a minimum axial force coefficient and minimum fluctuating pressure level over a range of flight conditions seen in a typical launch trajectory. The effects of axial forces are only significant during the early part of the launch trajectory and

problems caused by pressure fluctuations are usually seen during the ascent phase and during maximum dynamic pressure. For this reason only flight conditions up to approximately 50,000 ft were considered, where pressure and density are about 11% and 15% respectively of sea level conditions in a standard atmosphere. The launch vehicle ascent trajectory used for this study is shown in Figure 3, showing altitude and dynamic pressure as a function of Mach number. This ascent trajectory is similar to that of the Saturn V launch vehicle.⁴¹

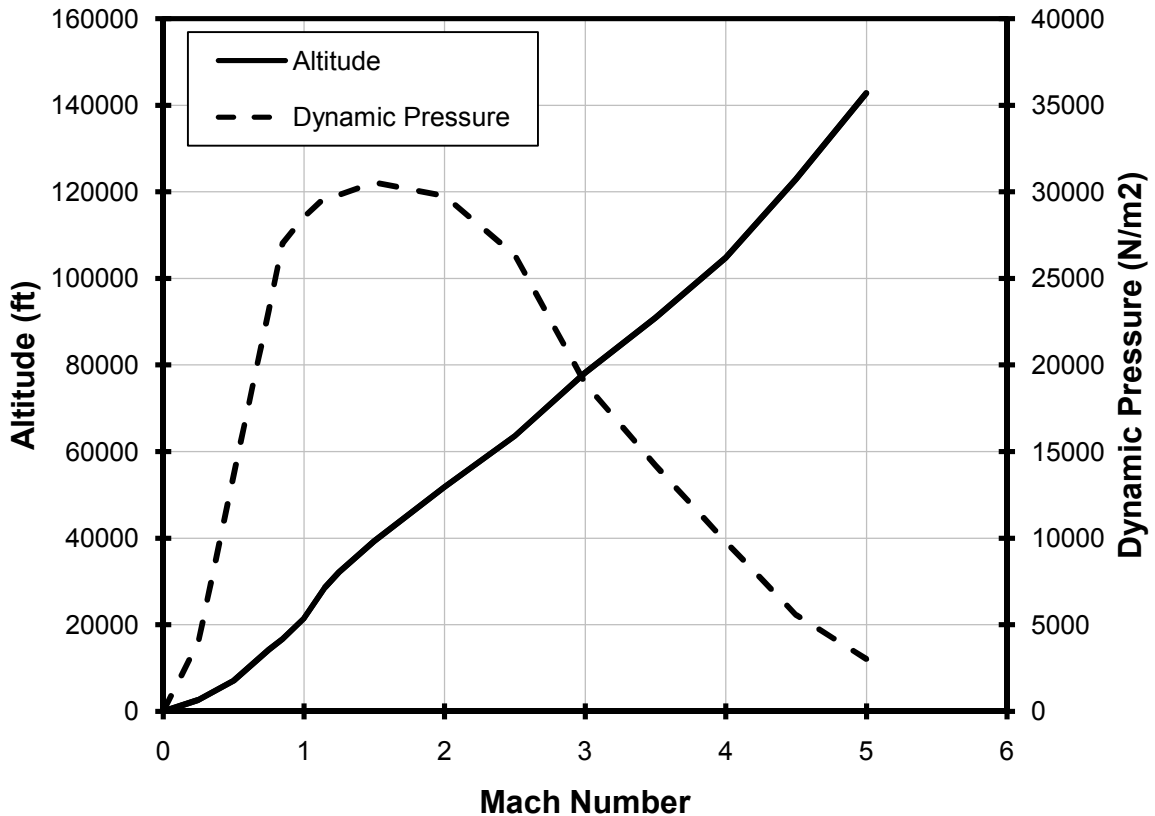


Figure 3: Altitude and Dynamic Pressure as a Function of Mach Number

It is important to include the condition of maximum dynamic pressure since axial force is generally high during this flight condition. For this ascent trajectory the

maximum dynamic pressure condition occurs at a Mach number of approximately 1.50 and an altitude of about 39,300 ft. Also, since pressure fluctuations are generally high during transonic flight due to shock instabilities, it is important to include flight conditions near the transonic flight regime. While it would be best to include all the flight conditions in the trajectory, it would not be practical due to the extensive amount of time it would take to run every flight condition through the CFD solver. For this reason only five conditions are modeled in this study. The exact flight conditions considered for this study are shown in Table 2.

Table 2: Flight Conditions Considered During the Ascent Trajectory

<i>Flight Condition</i>	<i>Mach Number</i>	<i>Altitude</i>	<i>Temperature</i>	<i>Pressure</i>
1	0.50	7100	274.08	77889
2	0.85	16667	255.13	53445
3	1.15	28600	231.49	32058
4	1.50	39300	216.65	19396
5	2.00	51800	216.65	10636

2.3 CFD MODEL

The CFD solver used for both the pressure fluctuation level and axial force minimization studies was the Fluent CFD solver. The solver is operated on a Linux cluster of microprocessors that has a total of 30 nodes where each node consists of two AMD Opteron 242 (64-bit) chips for a total of 60 processors. Fluent is a robust CFD software package with a wide range of capability for modeling fluid flow. For both studies the Fluent CFD software solves the steady-state Reynolds-Averaged Navier-Stokes (RANS) equations using a cell-centered finite-volume method for integration. The

RANS equations allow for a solution of the mean flow parameters with a reduced computational expense compared to other methods such as Large Eddy Simulation (LES). The Reynolds-Averaged approach is commonly used for many practical engineering applications.

Both CFD models use an axisymmetric segregated solver such that the momentum and continuity equations are decoupled. The fluid was modeled using Fluent's built-in properties for air where density was modeled assuming an ideal gas. Also, the energy equation is activated, since the modeled trajectory goes through a range of high-speed compressible flow conditions.

To more accurately model the flow around the vehicle, a built-in turbulence model was used. There are several different options within Fluent for modeling turbulence, however the $k-\varepsilon$ turbulence model was deemed suitable for this study as it is widely used for both incompressible and compressible flows. The $k-\varepsilon$ model is a two equation turbulence model that includes the turbulent kinetic energy, k , and the turbulent dissipation rate, ε . While there are a variety of $k-\varepsilon$ turbulence models, such as the Renormalization Group (RNG) and Realizable approaches, the standard $k-\varepsilon$ model was employed for this study.

2.4 MESHING THE MODEL

The grid generator is a FORTRAN routine that develops a structured mesh based on the variables that define the geometry. To clearly show the structure of the mesh a very coarse mesh for the model is illustrated in Figure 4. The entire mesh is structured and contained in one zone. Indexing starts at the nose of the model and extends to the

right for the increasing i direction and outward from the wall for the increasing j direction. The most difficult part of programming the grid generator was mapping the nodal points to provide an adequate mesh while also avoiding grid overlap. Due to the model geometry and the use of a structured grid a region of potential grid overlap can occur. This region is indicated by the dashed oval in Figure 4. Grid overlap becomes more difficult as the angle of the first conic section becomes larger. Grid overlap is avoided in the grid generator by mapping the nodal points so that the grid lines extending in the j direction away from the wall gradually curve away from the region of potential grid overlap.

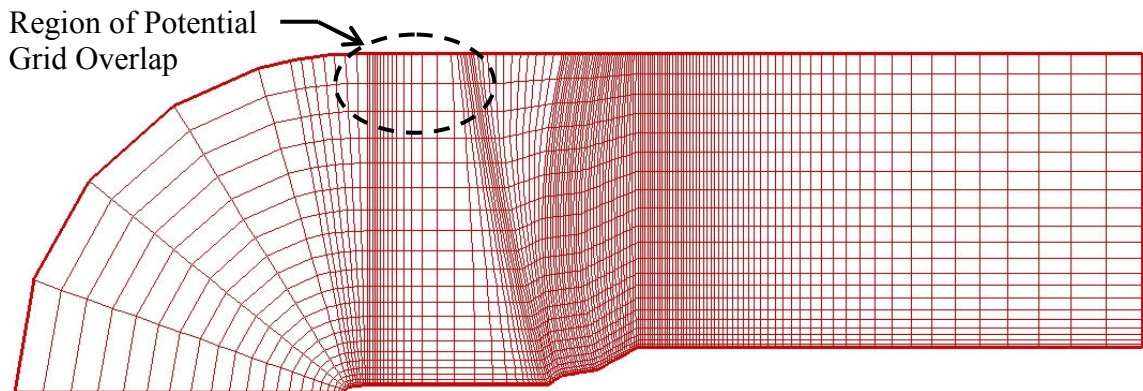


Figure 4: Example of Launch Vehicle Mesh

Other regions of interest in the mesh are the nose, the conic sections, and the nodal point distributions along the cylindrical sections in the i direction. The nodes near the nose and conic sections of the model are kept very dense due to the pressure gradients seen in these areas. Spacing in the i direction for both the nose and conic sections is held at the same constant value. This spacing value is determined by specifying the number of points along the first arc of the nose. The nodal points are kept perpendicular to the wall

throughout the nose section; however this is not possible for the small cylindrical section or the conic sections. A close-up of the very course mesh near the conic sections is shown in Figure 5. This figure also shows more clearly how the grid lines in the j direction gradually curve as the nodal points get further away from the wall. The points extending from the wall near the conic sections are kept near perpendicular and can be seen in Figure 5.

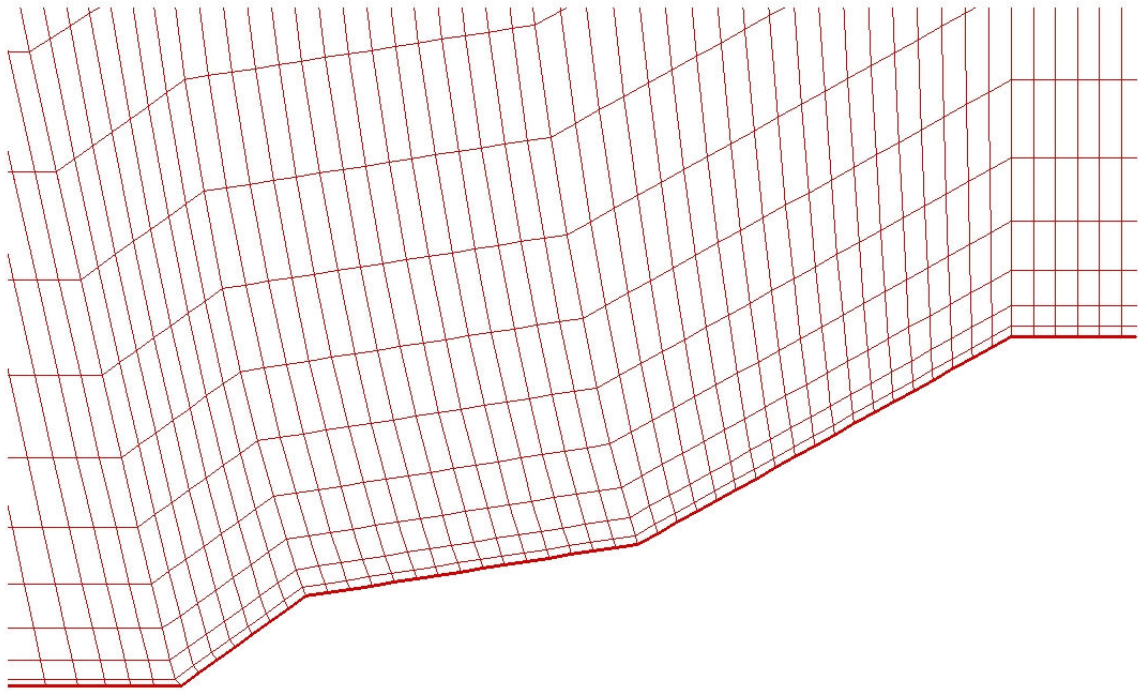


Figure 5: Close-up of Grid Near Conic Sections

An attempt is made to reduce the number of unnecessary elements by varying the spacing of points along the cylindrical sections. A cosine distribution is used for the small cylindrical section such that the nodal points are close together near the nose and first conic section whereas the points are much more spaced out through the middle of the section. A cosine distribution is also used for the large cylindrical section however the function is modified such that the spacing of the points are close together near the end of

the conic sections and gradually become more spaced out as the points get near the end. Since for this study the impact on the axial force coefficient from only the forebody of the vehicle is of interest, the aft end is not included in the model.

Spacing of nodal points in the j direction is controlled using a hyperbolic tangent function. This function allows for variable spacing of the nodal points in the j direction. The function is set up such that nodal points near the wall are spaced very closely together while the spacing gradually increases as the points get further out from the wall. This allows for adequate grid resolution near the wall while not having excessive element density far from the wall. The maximum distance from the wall deemed to be adequate for this flow field is seven large cylinder diameters in the j direction. To determine the first point from the wall the Near Wall Model is implemented. This model consists of approximating the skin friction coefficient to estimate the shear stress at the wall. With the estimated shear stress the friction velocity can be calculated, which allows the normalized turbulence length y^+ to be determined as a function of the distance y normal to the wall. Setting y^+ equal to one and solving for y gives an appropriate distance for the first nodal point from the wall. This method is similar to that used in reference 39 and 40.

2.5 GRID REFINEMENT STUDY

A grid refinement study was conducted on the model for a fixed geometry to ensure accurate results. This fixed geometry is also considered the baseline shape for this study. The number of nodal points in both the i and j directions were varied to obtain a course mesh and a fine mesh. Table 3 shows the different mesh sizes and Figure 6 shows a comparison of the two meshes investigated in the grid refinement study. The two images

on the left side of the figure show the nose and conic regions for the course mesh while the two images on the right show the nose and conic regions for the fine mesh. The goal of this refinement study was to verify that no substantial change in axial force coefficient existed for the different meshes.

Table 3: Mesh Sizes Considered for Grid Refinement Study

	i_{max}	j_{max}	Number of Cells
Course Mesh	476	49	22800
Fine Mesh	660	84	54697

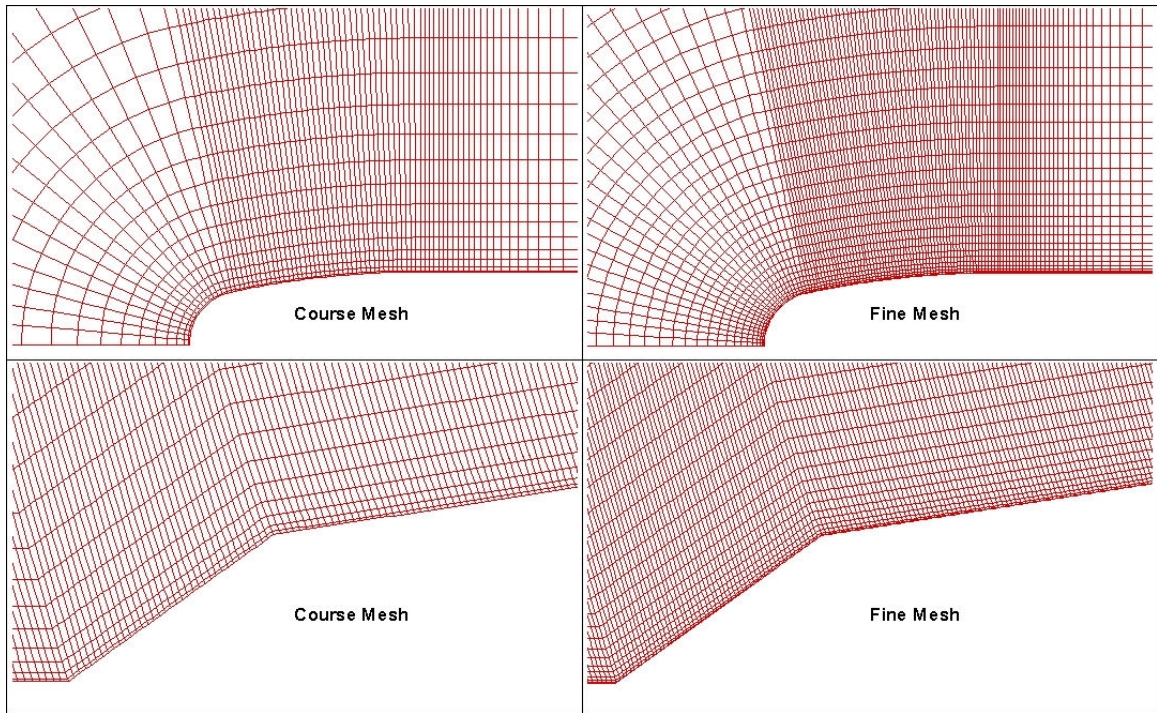


Figure 6: Comparison of Course and Fine Mesh

As mentioned previously, one of the goals of this optimization study is to minimize axial force over a range of flight conditions. The grid refinement study was carried out by running both meshes through the CFD solver over the range of flight conditions

considered in this study. To compare the results for each grid, the mean axial force coefficient for all flight conditions was plotted as a function of iteration. Figure 7 shows the mean axial force coefficient as a function of iteration for both meshes considered in the refinement study.

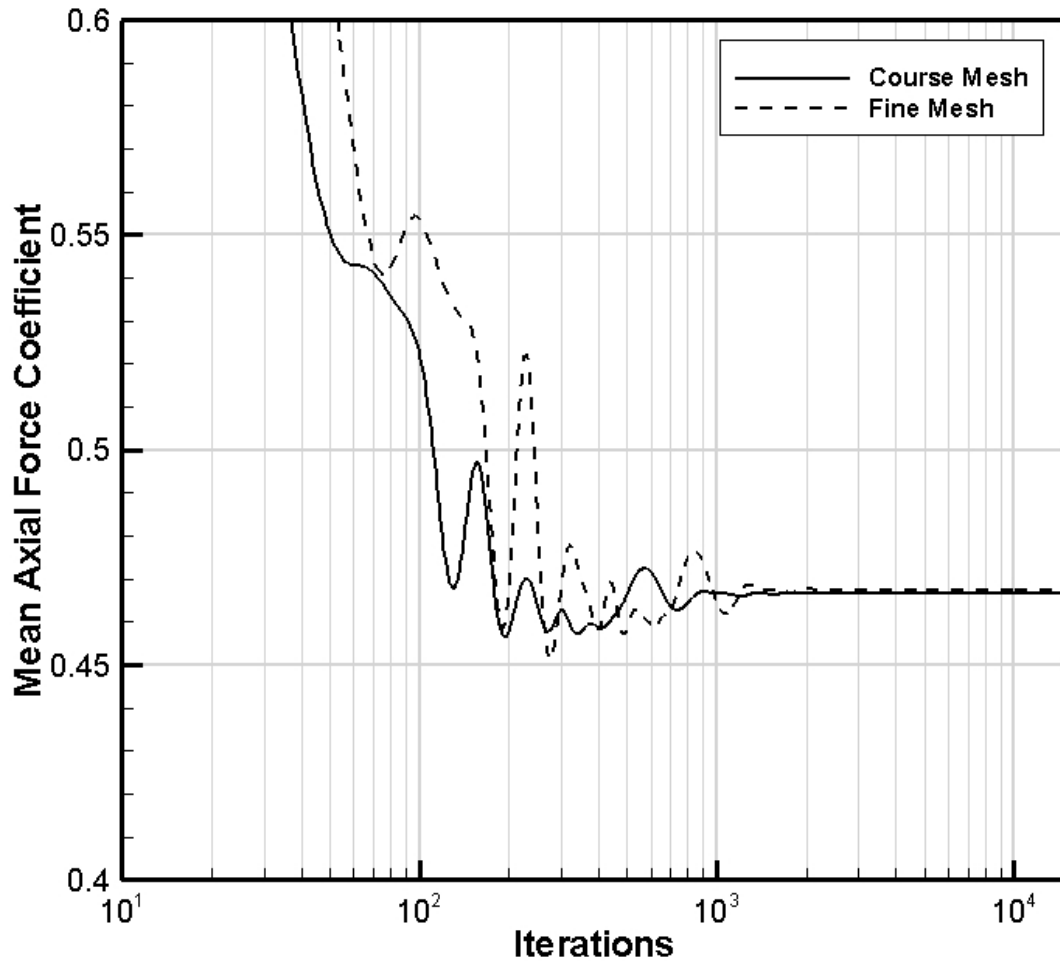


Figure 7: Axial Force Convergence for Considered Meshes in Refinement Study

Both meshes were allowed to run for 15000 iterations for all flight conditions. Figure 7 shows that both meshes converge to a mean axial force coefficient near 0.467 where the fine mesh gives an axial force coefficient just slightly higher than that of the course mesh. This difference is insignificant for this study since obtaining the exact axial

force coefficient is not the primary concern but rather finding a geometric shape with a minimum axial force is the goal. Also Figure 7 shows that the mean axial force coefficient for both meshes is sufficiently converged near 1100 iterations. Since the axial force varies as a function of flight Mach number it is important to ensure that there is also no significant difference in the axial force coefficient for each flight condition. Figure 8 shows the axial force coefficient through the prescribed flight conditions for both the course and fine meshes. It is shown from this figure that no significant differences exist in the axial force coefficient throughout the ascent trajectory for the two meshes. In addition to Figure 7 and Figure 8 the computation time to compute 15000 iterations for both meshes at each flight condition is displayed in Figure 9.

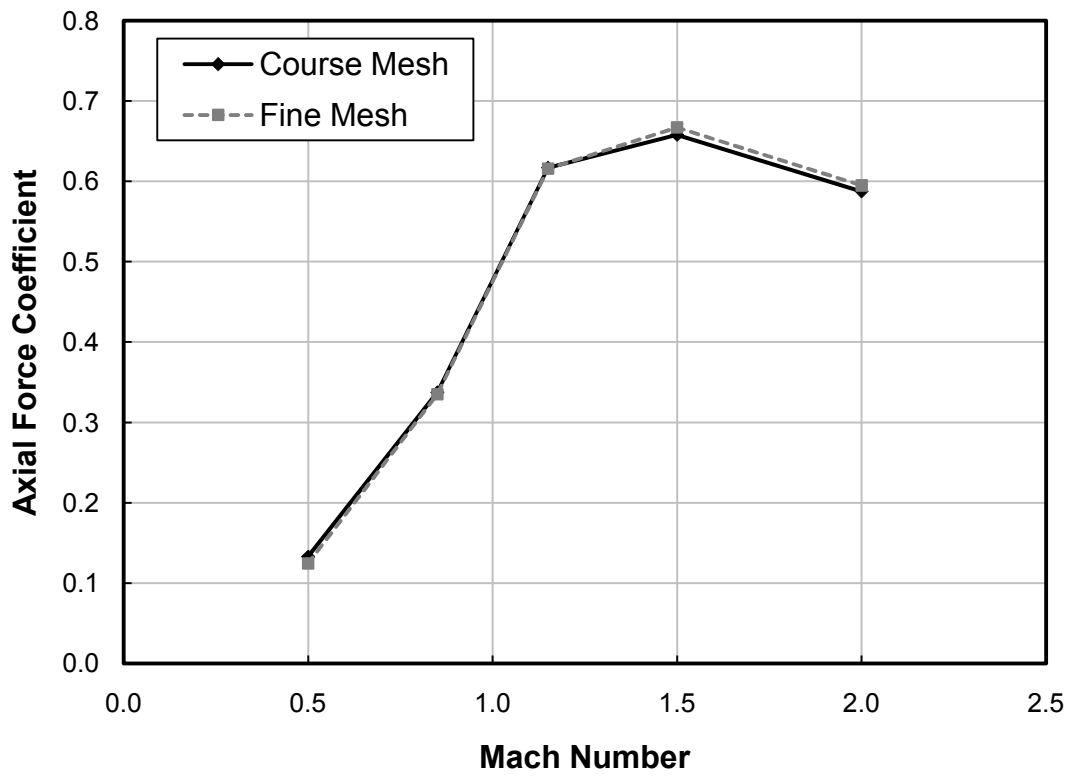


Figure 8: Axial Force Coefficient Throughout Ascent for Course and Fine Mesh

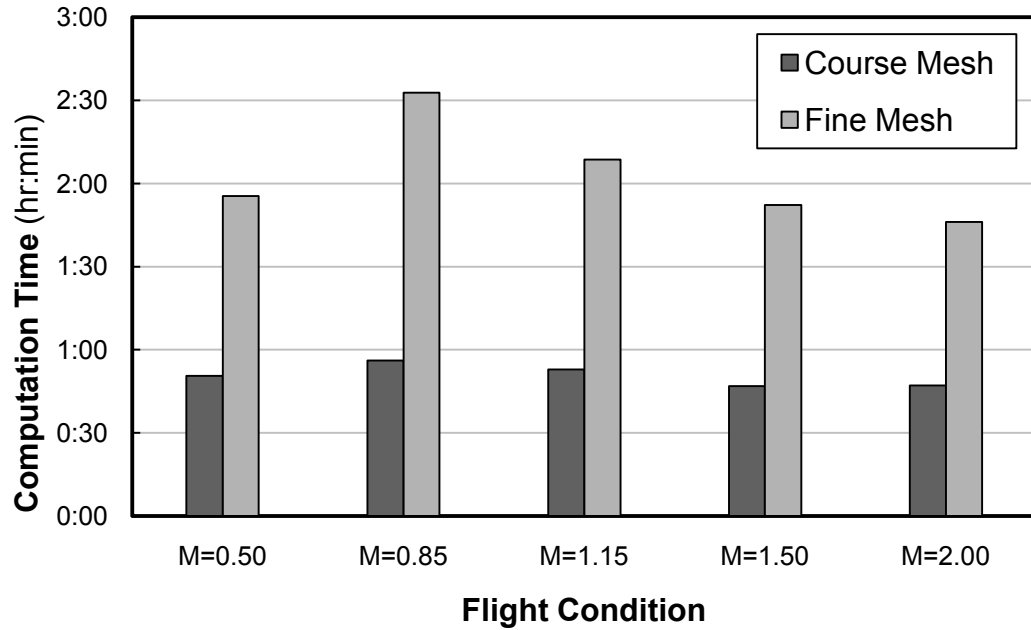


Figure 9: Comparison of Computation Times at Each Flight Condition

Figure 9 shows a substantial increase in computation time for the fine mesh compared to the course mesh. For most flight conditions the fine mesh took over twice as long as the course mesh to solve. Due to the extensive run time of the fine mesh and insignificant difference in axial force coefficient between the course and fine mesh, the course mesh was chosen to be most suitable for this study. Figure 9 also shows that the computation time for the Mach 0.85 condition took the longest to compute. This indicates that this flight condition is the most difficult case for the Fluent CFD solver to resolve. To further validate the use of the course grid over the fine grid the pressure distribution is compared for both grids. Figure 10 and Figure 11 show contour plots of the pressure distribution near the conic sections at the Mach 0.85 flight condition for the course and fine grids respectively. Comparison of these two figures clearly shows that no significant difference exists in the pressure distribution for the course and fine grids. Note that the

pressure values displayed in these images is in gauge pressure where zero pressure is the ambient flight condition.

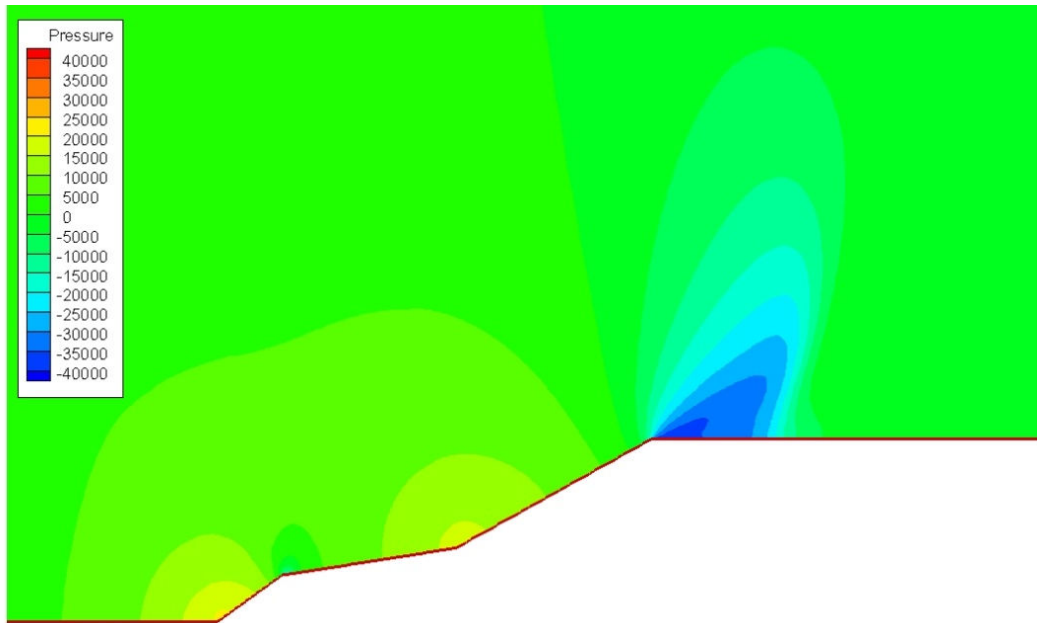


Figure 10: Pressure Distribution Plot for Course Grid

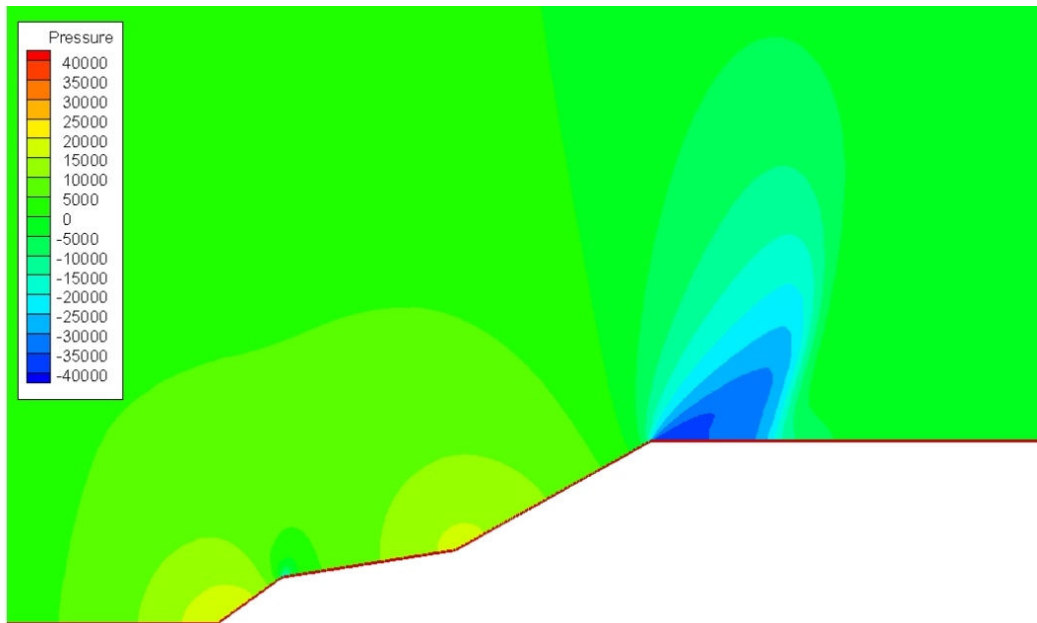


Figure 11: Pressure Distribution Plot for Fine Grid

2.6 PRESSURE FLUCTUATION MODEL

The pressure fluctuation level was calculated at only one point on the geometry. This point is approximately $0.25m$ aft of the third conic section as shown in Figure 12. This point was chosen because it was suspected to experience the highest levels of pressure fluctuations on the baseline geometry. The fluctuating pressure level was calculated at this point based on several local and freestream flow parameters. The parameters include freestream Mach number, freestream and local dynamic pressure, local velocity, local density, viscosity and Reynolds Number. Note that what is meant by freestream is actually global freestream, not the condition at the edge of the boundary layer. For this study, the flow parameters at the edge of the boundary layer are referred to as the local flow parameters at the point of interest.

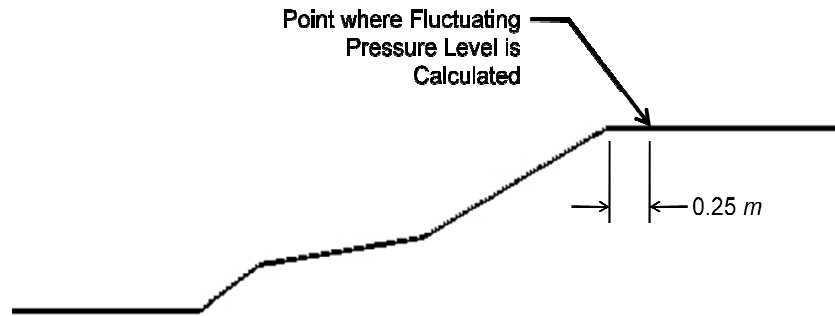


Figure 12: Location of Pressure Fluctuation Level Calculation

While the freestream flow parameters are given for each flight condition, extracting the local flow parameters at the point of interest is a nontrivial exercise. This is due to that fact that the boundary layer thickness is dependent on the geometry and vehicle flight speed. So simply investigating the local flow field at this point for a given flight condition and assigning a height above the surface to sample local flow parameters will not suffice. For supersonic freestream Mach numbers, an expansion fan develops such

that the flow is accelerated around this corner. During subsonic flight the acceleration of the flow is not as pronounced. The effect that flight speed has on the local flow velocity is shown by Figure 13 in which the flow velocity is plotted versus the distance from the wall. Only three of the five flight conditions are shown in this figure to demonstrate the effect flight speed has on the local velocity profile.

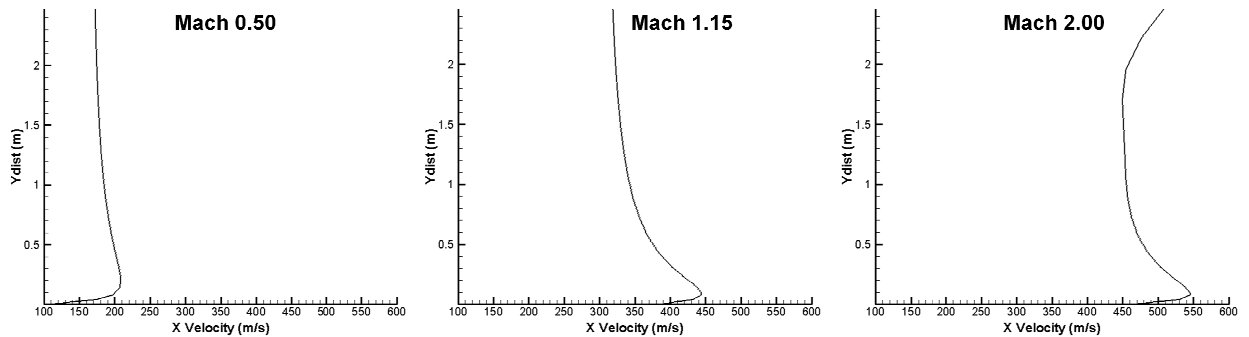


Figure 13: Effect of Flight Speed on Velocity Profiles

It is desired to take the location of the peak velocity as the sample point for local flow parameters from the CFD data as it is believed that this peak velocity has the largest effect on the fluctuating pressure level. This location is not only dependent on flight speed but also on the geometry. Since the GA can generate any combination of geometric variables within the design space, this point can move relative to the GA selected variables. A method had to be implemented into the objective function for communicating to the CFD solver the coordinates of this location. This was done by modifying the batch file used by the CFD solver to execute commands for each member. In the grid generator routine, the x and y location of the corner point is passed to another routine for writing the batch file. The x location where the pressure fluctuation level is calculated is $0.25m$ aft of the corner x location. An equal distribution of 25 points is extended from the surface at this x location to a distance of $0.75m$ above the surface.

Upon solution convergence the CFD solver extracts the local flow parameters at these 25 points and records the data in an output file. This data is then read by another FORTRAN routine which determines the point at which the peak velocity occurs and calculates the local flow parameters based on given CFD data at that same point.

The pressure fluctuation prediction model implemented into this optimization study is shown in the equation below. This is a physics based model that calculates the RMS pressure fluctuation level and has been developed by curve fitting flight data of fluctuating pressure levels for several different launch vehicles. This model has been shown to provide adequate correlation to flight data for a similar location on similarly shaped launch vehicles. For proprietary reasons, the actual flight data along with the curve fitting results cannot be provided. It should be noted, however, that it is not the intent of this study to provide a highly accurate model for calculating pressure fluctuations. A More robust model for pressure fluctuations can be implemented into this optimization process with relative ease. This particular model was chosen for this study as it was readily available to the author.

$$\frac{\sqrt{p^2}}{q_\infty} \cong (\text{Re})^n \left[A * \left(1 + \frac{\gamma - 1}{2} M^2 \right)^N \right] \times \frac{q_\infty}{q_{local}} + \left(\frac{\beta}{(b - M_\infty)^2 + \xi M_\infty^2} \right)$$

3 LAUNCH VEHICLE OPTIMIZATION

3.1 CODE STRUCTURE

The code structures for the axial force minimization study and the pressure fluctuation minimization study were very similar. The optimization process for a typical GA is shown in a diagram in Figure 14. The GA starts with the first generation of members by randomly selecting variables within the prescribed design space. In this case, each member represents a particular set of geometric parameters which define the shape of a launch vehicle resembling the Ares I Crew Launch Vehicle. Each member is passed one by one to the objective function where a grid is generated based on the geometric parameters. This grid is then sent to a CFD solver where the axial force coefficient is calculated for that member. Once a generation is completed each member is ranked according to its performance relative to other members in the same generation. This ranking system determines the selection of variables for the next generation. This process is repeated until all generations are completed. For this study 30 members were evaluated over 20 generations. The goals of these optimizations are to minimize the average axial force coefficient and fluctuating pressure level for the launch vehicle throughout several flight conditions in a typical launch trajectory.

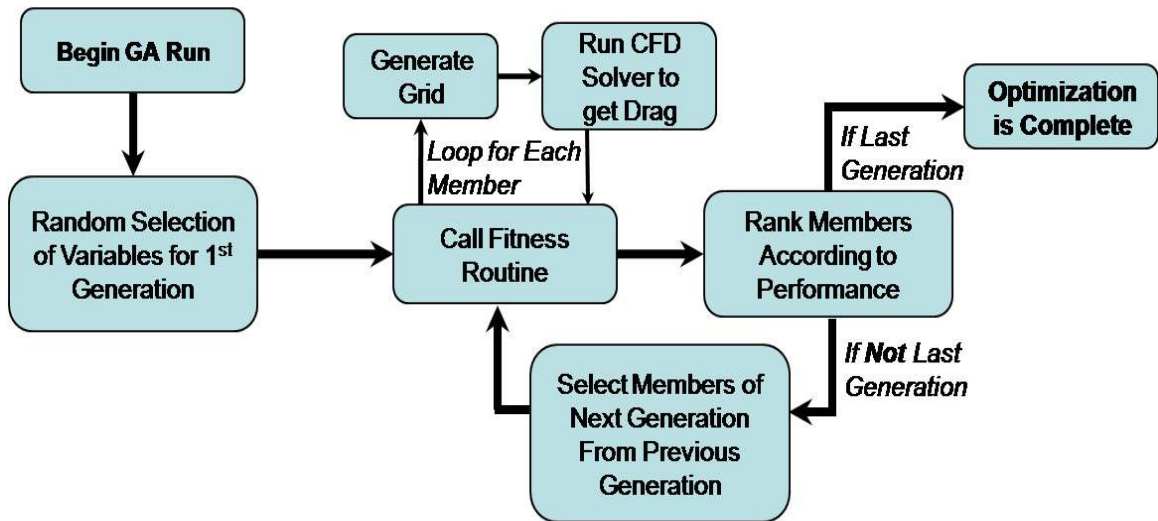


Figure 14: Flow Diagram for a Typical Genetic Algorithm

An effort was made to reduce computational expense by having each CFD run parallelized by the Fluent solver on a Linux cluster maintained by Auburn University. The Linux cluster houses 30 nodes where each node contains two AMD Opteron 242 (64-bit) chips for a total of 60 processors. For this study each CFD run was distributed across two nodes (four processors). With this approach the average computation time for each member to be solved at all five flight conditions by the CFD solver was approximately 3.25 hours. Running the member sequentially for 30 members over 20 generations would result in a total GA run time of about 1950 hours or over 80 days. This is far too long of a run time for this study, so methods had to be implemented in order to substantially reduce the computational expense.

A method for greatly reducing the GA run time was implemented into this study and was developed by Doyle.⁴⁰ This method consists of running multiple members simultaneously while each member was parallelized by Fluent. This works by essentially running a script file that executes Fluent after the mesh for a particular member has been generated. This script file allows Fluent to be executed in the background so that the GA

can continue and load in another member instead of waiting for the previous member to finish. Multiple slots were allotted for members to occupy where no more than one member could occupy a slot. However, steps must be taken to ensure that multiple members are not started simultaneously. This is handled by essentially suspending the program in a loop for a brief period to allow the previous member time to initialize. More details explaining this modification to the GA is discussed in reference 40. Figure 15 shows a flow chart for the optimization process running multiple members simultaneously.

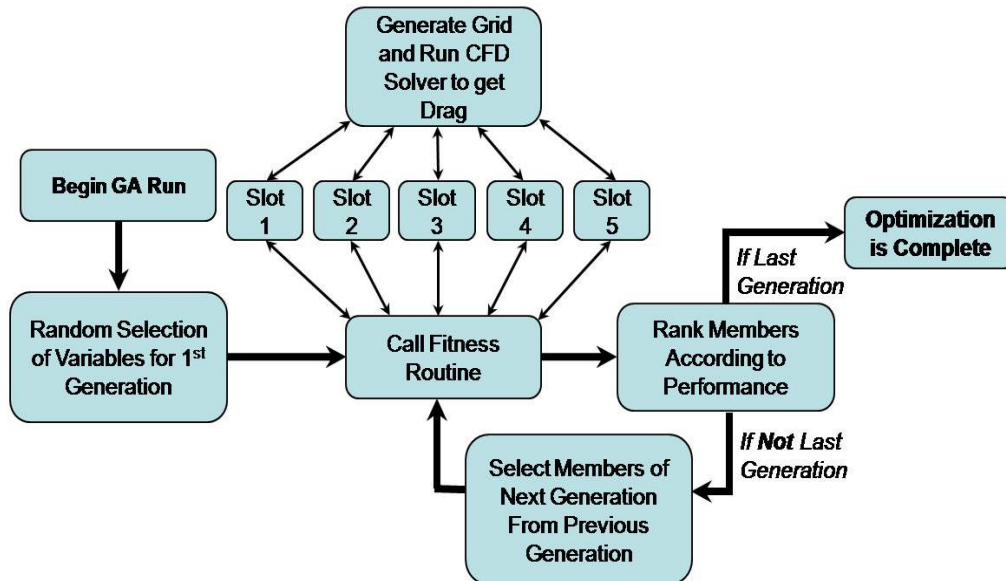


Figure 15: Flow Diagram for GA Running Multiple Members Simultaneously

For this study 10 slots were allotted so that 10 members could be run simultaneously. At the beginning of a generation the first 10 members of the generation were loaded into all the slots one by one. After the first ten were loaded the GA began to check for the completion of a member. Once the GA detected that a member was finished the GA would load in the next member. This process would repeat until all members in that generation were complete. This method of running multiple members simultaneously

significantly reduced the total GA run time. With 10 members running at once and 30 members over 20 generations the total GA run time was cut down to approximately 225 hours or just over 9 days.

Table 4 shows the design space for this study and is the same for both optimization studies. Limitations had to be placed on the design space to prevent impractical geometries from being generated, such as having the first cone radius larger than the second cone radius, or having a very large cone angle. This was partially handled by defining the second cone radius, $Rc2$, to be a percentage of the base radius, Rb , and the first cone radius, $Rc1$, being a percentage of the $Rc2$. Preventing large cone angles was not as easily handled as there are many combinations of design parameters that could produce a large cone angle. It was important, however, to eliminate the possibility of producing geometries with large cone angles as it was found that at supersonic Mach numbers the CFD solver would diverge for large cone angles which would cause the GA run to crash. To eliminate this possibility a check was placed in the grid generator to check that the angle of each cone was less than 60° . If a cone angle was found to be larger than 60° the CFD solver would not be executed and the axial force coefficient would be forced to a large number so that the GA would see that member as a bad set of design variables.

Table 4: Prescribed Design Space for Both Optimization Studies

<i>Parameter</i>	<i>Minimum</i>	<i>Maximum</i>	<i>Increment</i>
Rc1	0.50	1.00	0.02
Rc2	0.40	0.99	0.02
LcTot	1.50	3.00	0.05
Lc1	0.05	0.35	0.01
Lc3	0.10	0.60	0.01

3.2 PRESSURE FLUCTUATION MINIMIZATION STUDY

3.2.1 CONVERGENCE CRITERIA

The RMS fluctuating pressure level is the parameter of interest for this study and it would be ideal to monitor CFD solution convergence based on this parameter. However, Fluent does not have the option of calculating and monitoring the pressure fluctuation level so the local pressure at this point of interest was monitored. Fluent is unable to monitor solution convergence based on pressure so it was necessary to investigate the value of the residuals for continuity, x -momentum, y -momentum, energy, k , and ε when the local pressure was sufficiently converged. From the grid refinement study in the previous chapter it was shown that the course mesh was deemed suitable for both optimization studies. For this reason, only the convergence criteria for the course mesh using the baseline geometry will be investigated.

As indicated in the previous chapter by Figure 9 the Mach 0.85 flight condition was the most difficult condition for Fluent to resolve, so this condition was used to determine the convergence criteria. This flight condition was run for 15000 iterations to allow for more than enough time for the CFD solver to obtain a converged solution. Figure 16

shows the residuals and local pressure plotted against the number of iterations. This figure shows that the residuals have completely converged around 6000 to 7000 iterations. The local pressure, however, converged much sooner at less than 2000 iterations. At 2000 iterations all the residuals had converged to 10^{-6} or lower, except for the continuity residual, which had converged to approximately 10^{-5} . To ensure adequate convergence of the local pressure, the solution was deemed converged once all the residuals reached 10^{-6} within a maximum of 10000 iterations. If a particular member did not meet this convergence criterion then that member was disqualified by setting the RMS pressure fluctuation level to an extremely high value of 1000.

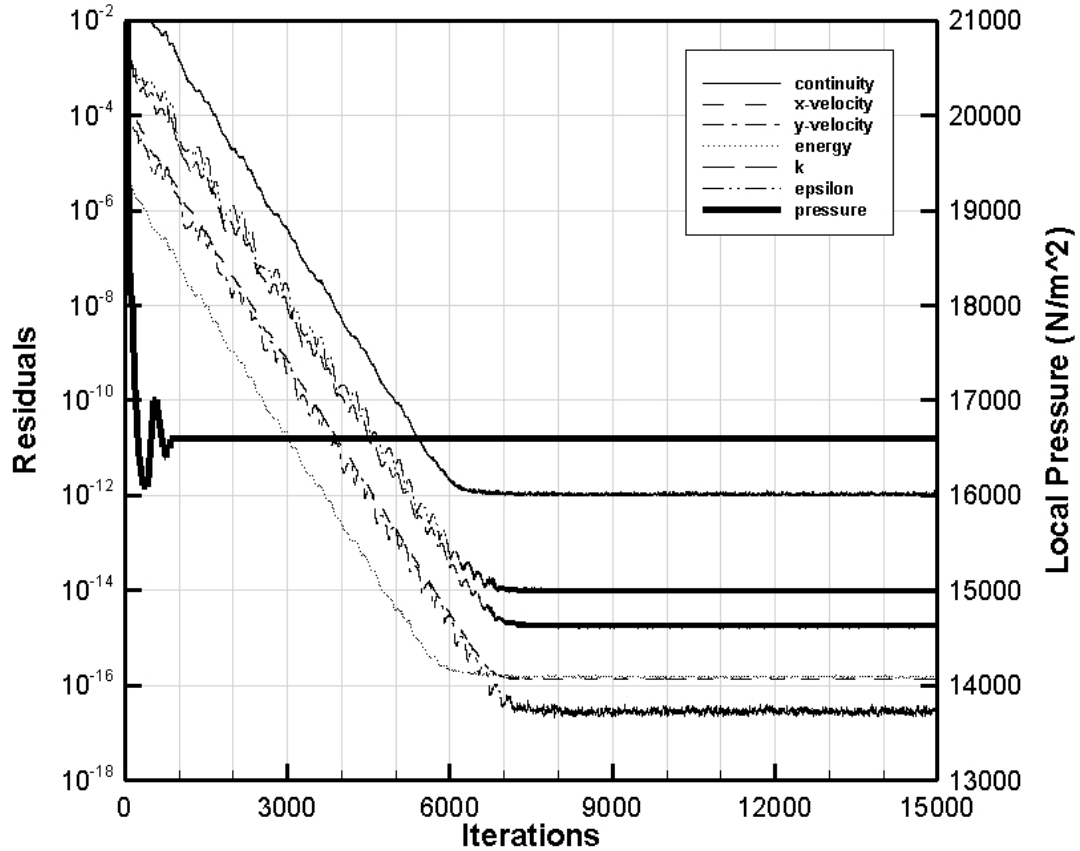


Figure 16: Residuals and Local Pressure Convergence for the Course Mesh and Mach 0.85 Flight Condition

Setting an extremely high performance penalty for a particular member of externally understandable characteristics essentially eliminates the traits that cause the CFD solver difficulty in obtaining converged solutions. The negative impact of this disqualification is that it eliminates members due to problems with solution convergence, and not because of high pressure fluctuations. This means that there is a possibility that the GA could eliminate a potentially good performer. Further study could be done to determine if the disqualified members could produce good performance; however this would require a great deal more time that is beyond the scope of this study as this study

aims to demonstrate a methodology for reducing the fluctuating pressure level of launch vehicles.

During trial GA runs it was recognized that the aforementioned convergence criteria was not sufficient for all the possible geometries allowed in the prescribed design space. It was noticed that for some members at certain flight conditions, the residual for continuity would converge to a value less than 10^{-6} thereby never actually meeting the convergence criteria. For these cases, however, it was noticed that the local pressure was sufficiently converged. This resulted in the GA eliminating potential good members that had converged solutions. The solution to this problem was to develop an additional convergence criterion. This criterion was a check to see if the local pressure had sufficiently converged even if the residual convergence criterion was not satisfied. The local pressure was deemed converged if the value was found to not differ by more than 0.1% over the final 2000 iterations. If the member failed this pressure convergence criterion, then the member was disqualified by setting the RMS pressure fluctuation level to a high value. This essentially disqualifies the member as discussed previously.

3.2.2 PRESSURE FLUCTUATION MINIMIZATION RESULTS

The average fluctuation pressure level throughout the ascent trajectory for the baseline model was calculated to be 0.0216. The optimized geometry gave a pressure fluctuation level of just 0.0178. This was approximately a 17.5% reduction from the baseline geometry. The GA was not able to significantly improve performance after the 1st generation however.

Figure 17 shows the fluctuating pressure level throughout the ascent trajectory for the baseline and optimized geometries. This figure shows that the pressure fluctuations for both geometries follow the same trend as a function of free stream Mach number where the fluctuation level for the optimized geometry stays fairly constant after Mach 1.15. After Mach 1.15 is where the optimized geometry sees the most improvement in performance over the baseline geometry. The Mach 0.5 and 0.85 flight conditions see little change where the optimized geometry actually has a slightly higher pressure fluctuation level for the first flight condition. The largest reduction in fluctuating pressure level occurs during the last flight condition of Mach 2.0, in which a 36.6% reduction was achieved. While a 17.5% reduction of the average RMS pressure fluctuation was achieved, there was only a 7.7% reduction in the peak RMS pressure fluctuation level. This result could be improved in a couple of different ways. One way would be to open up the design space to include more surfaces throughout the conic sections, thereby allowing more flexibility in the geometry. Another way that would likely improve this result would be to monitor only the Mach 0.85 flight condition where the peak fluctuation level occurs.

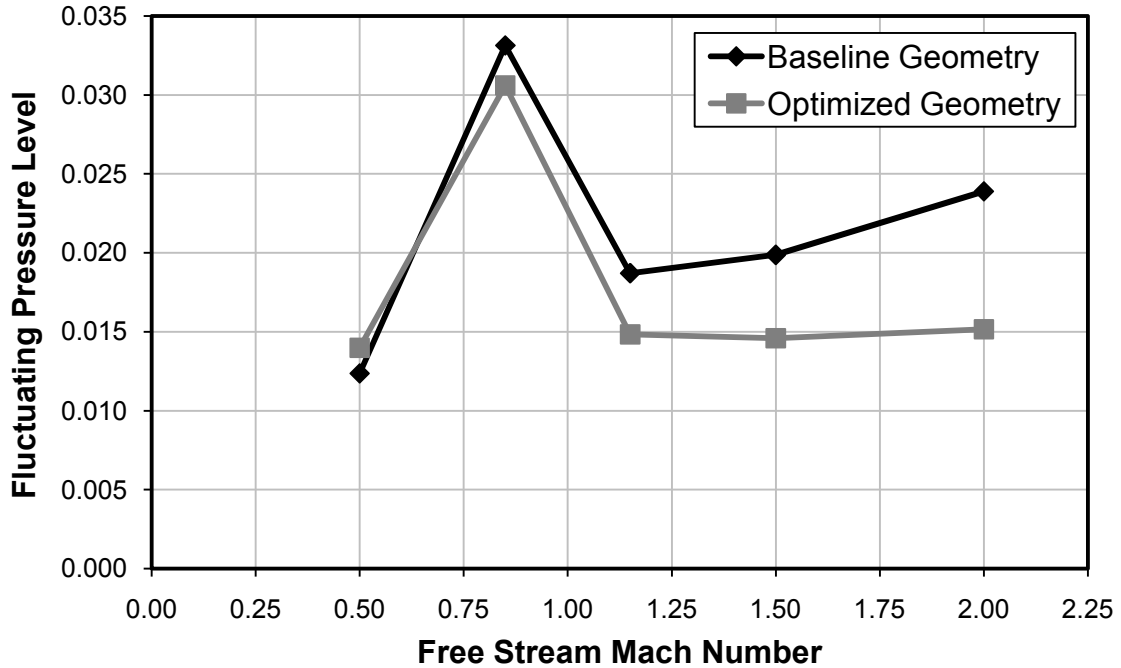


Figure 17: Fluctuating Pressure Level throughout Ascent for Baseline and Optimized Geometries

Figure 18 and Figure 19 show the evolution of the pressure fluctuation level throughout the total number of generations allowed for this optimization. Figure 18 shows how the maximum, average, and minimum pressure fluctuation members change for each generation. The erratic behavior of the maximum pressure fluctuation member is due to the GA's random manipulation of some of the population members. Figure 18 does not show any members that were disqualified. This is not because there were no disqualifications. The disqualified members were excluded from Figure 18 because there were so many. There were a total of 20 members that were disqualified, however not every generation produced a disqualified member. Several generations produced more than one member that was disqualified. The reason for the large number of disqualifications is due to the geometric shape the GA tended to favor. The GA had a

tendency to produce members with large first cone angles and very small second and third cone angles. So these disqualifications were due to the GA's selection of variables resulting in cone angles that exceeded the maximum angle allowed. No member was disqualified due to failing to meet the convergence criteria.

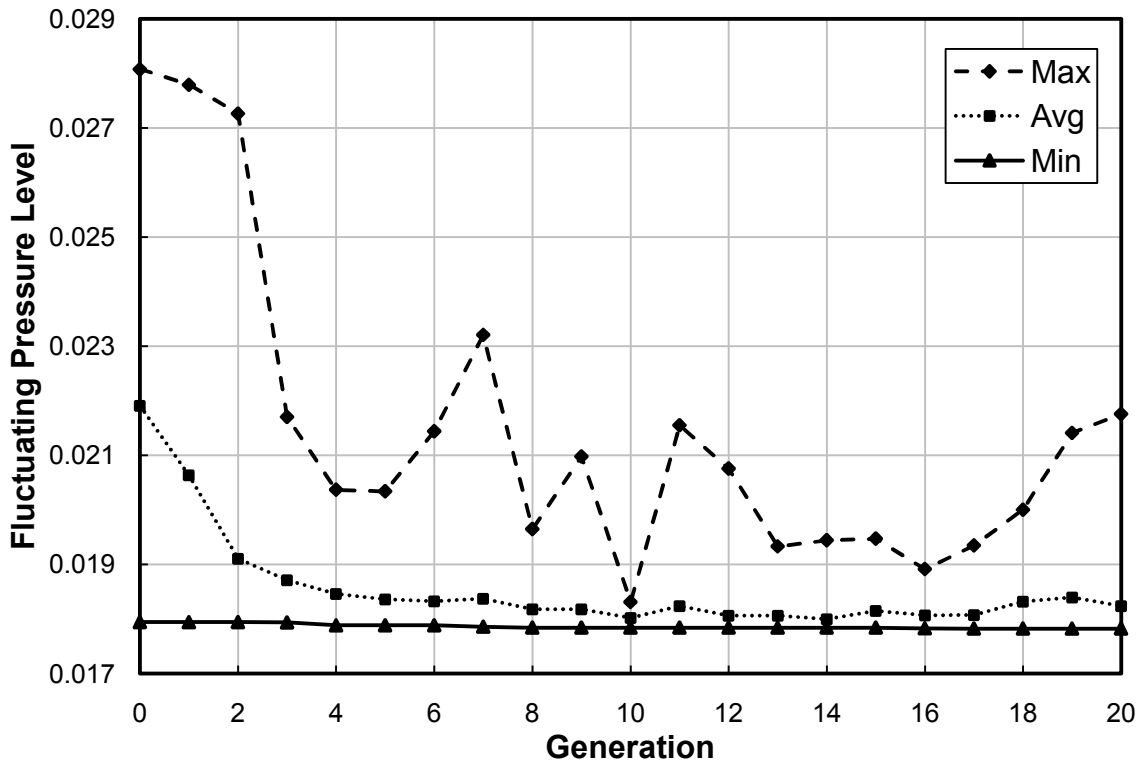


Figure 18: Maximum Average and Minimum Pressure Fluctuation Level Evolution

The results shown in Figure 18 show practically no change in the best performer throughout the generations. To more clearly show the improvement of the best performer throughout the generations, the best performer is shown separately in Figure 19. The GA was able to improve the best performer by only 0.66% from the first to the last generation. This indicates that the GA was able come very close to the optimized geometry in the initial generation by the random selection of members within the design space. The plot of the average performance member shows that the GA was able to

quickly learn what combination of parameters produced good performers. By about the eighth generation the average member performed nearly as well as the best performer.

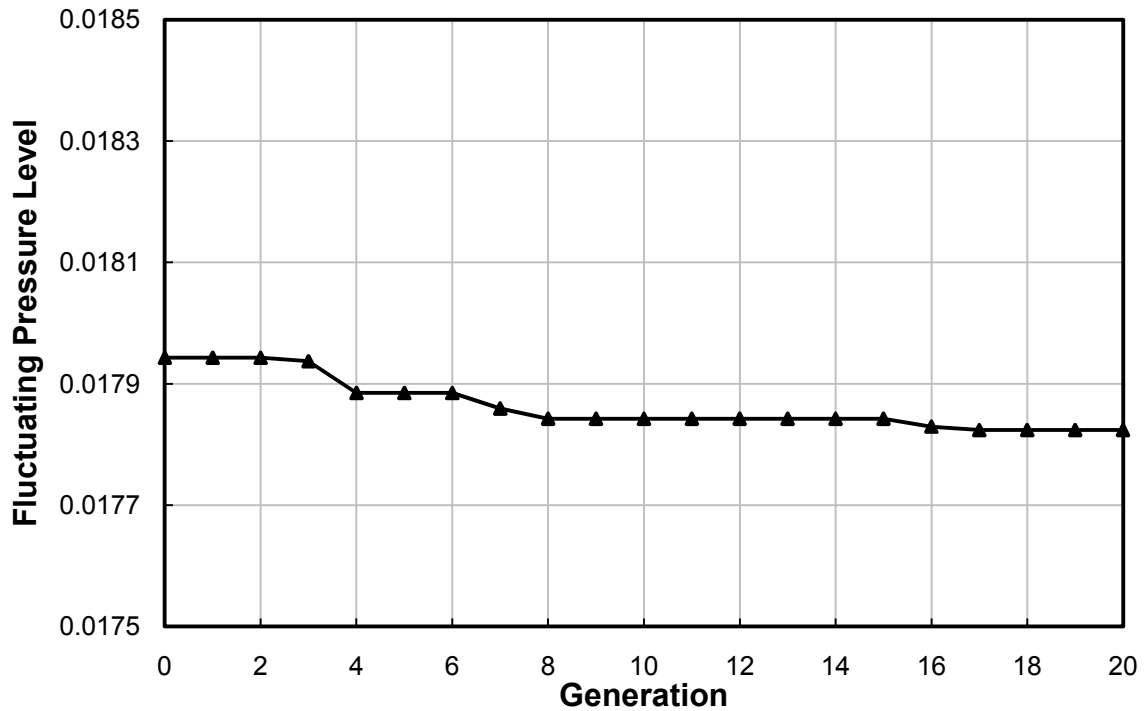


Figure 19: Minimum Fluctuating Pressure Level Evolution

Figure 20 shows the comparison of the optimized and baseline geometries. The first thing to notice about the shape optimized for minimizing the pressure fluctuation level is the large angle for the first conic section. While the shape still somewhat resembles a parabolic or blunted ogive shape the presence of the large cone angle makes this design undesirable overall. The reason for this result is because the fluctuating pressure level was monitored from only one critical point in the geometry. This point lies just aft of the point where the third conic section meets the large cylinder base section. As the optimized shape shows in Figure 20, the GA produced a shape that had a very small angle for the third conic section. With smaller cone angles for the third section, this would result is less flow separation which is a primary cause for high pressure

fluctuations. A new critical point would arise, however, just aft of the first conic section. Due to the large difference in the first and second cone angles flow separation occurs at this point for several of the flight conditions. While the overall optimized geometry would not be an ideal design due to the large angle of the first conic section, the methodology employed here has proved useful in minimizing the fluctuating pressure level at a critical point.

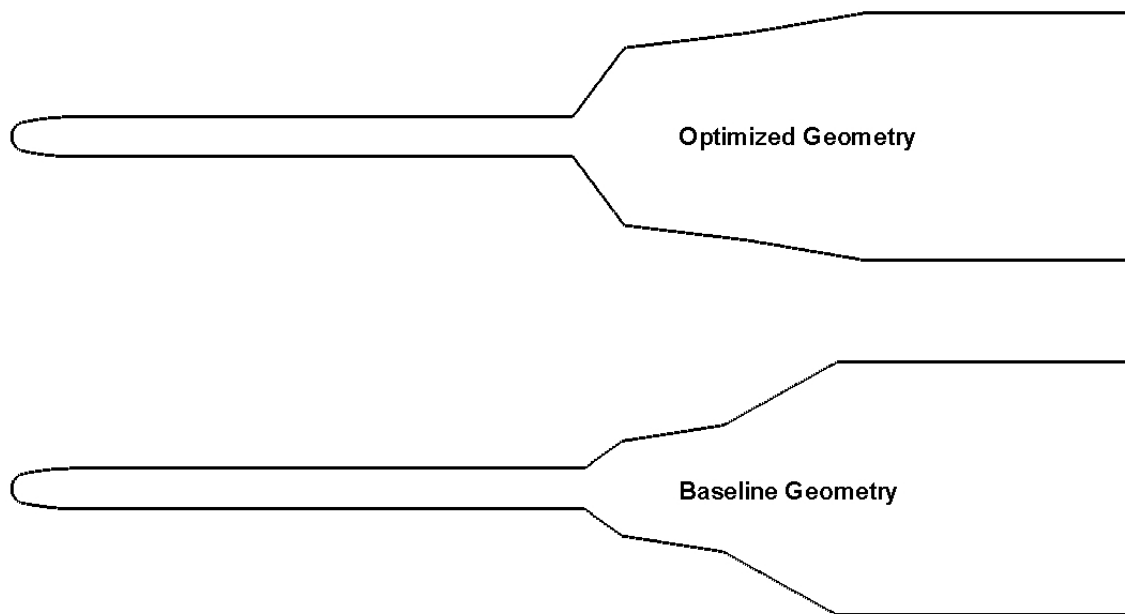


Figure 20: Pressure Fluctuation Level Study Geometry Comparison

Shown in Figure 21 through Figure 25 are the variable distribution plots for each GA variable. These plots show the GA’s selection of each variable for all the members in each generation within each parameter’s design space. Through these plots one can see the evolution of each design variable throughout the optimization process. For these figures the solid line represents the best performance member for each generation.

Figure 21 shows the variable distribution of the normalized *RcI* design variable. It can be seen that the GA begins in the initial or 0th generation with a fairly uniform distribution across the members. It appears that the majority of the members have normalized *RcI* variables in the upper half of the design space. This is just a coincidence since the population members for the initial generation are randomly generated by the GA. However, the GA does tend to produce members in the upper region of the design space. As can be seen from the solid line, the best performer is in the upper region for the entire optimization run. By the 8th generation the best performer has a normalized *RcI* variable of 0.855 and does not change for the remainder of the GA run. Such a large radius for the first conic section is the primary reason for such a large cone angle. This was an undesired result since such a large cone angle would generate high pressure fluctuation levels at a point just aft of the first conic section. This result could be avoided if fluctuating pressure levels were calculated for several points along the geometry.

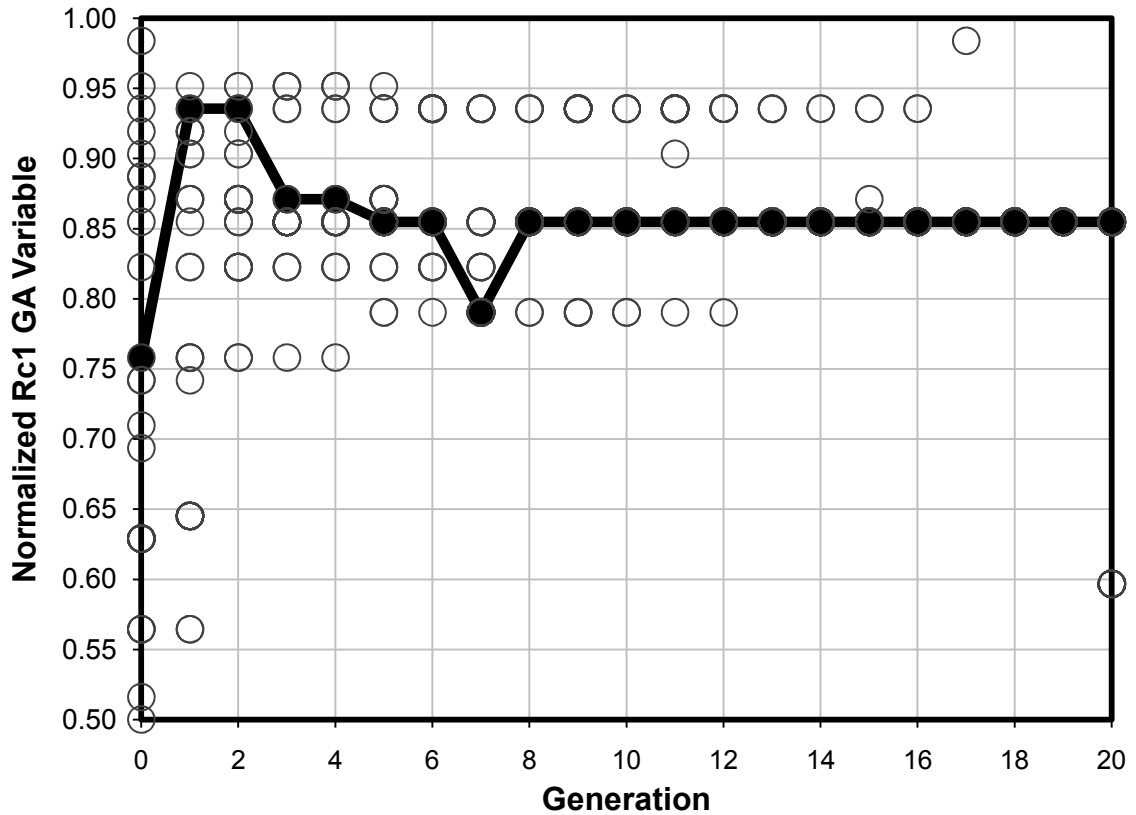


Figure 21: Pressure Fluctuation Study Variable Distribution for Rc1

The variable distribution for the normalized second cone radius, $Rc2$, is shown in Figure 22. The GA quickly narrows the selection of the $Rc2$ variable to the upper region of the design space. By the 5th generation the majority of the members are between 0.80 and 0.85. The best performer does not change after the 5th generation where the best performer had a normalized second cone radius of 0.838. Such a large radius for the second conic section was expected since the larger this radius is the smaller the angle is for the third conic section. With smaller angles for the third conic section, the flow is not accelerated as much over the point where the pressure fluctuation is calculated, which leads to lower fluctuating pressure levels.

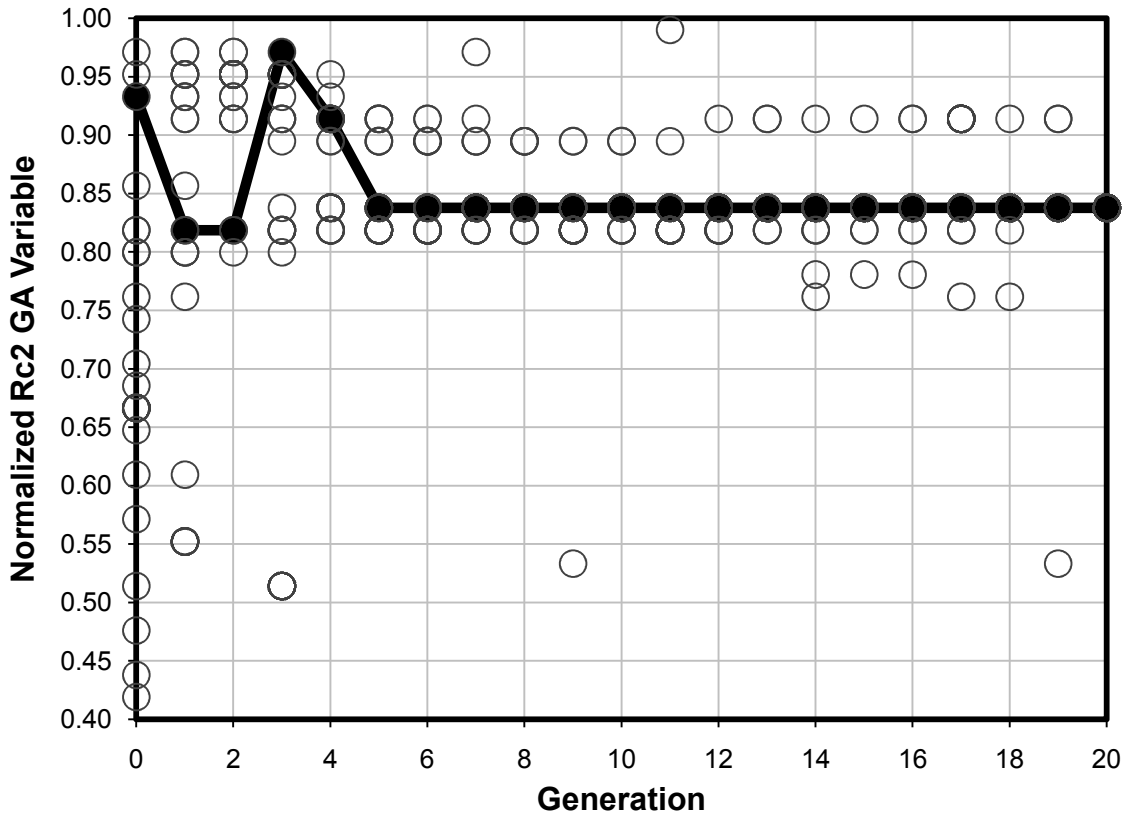


Figure 22: Pressure Fluctuation Study Variable Distribution for Rc2

Figure 23 shows the variable distribution for the normalized total length of the conic sections, $LcTot$. The GA's selection of the $LcTot$ variable tends to be fairly spread out in the design space for the first several generations. After the 5th generation a large majority of the members have a normalized $LcTot$ parameter of between 2.20 and 2.40. The $LcTot$ variable for the best performer stays constant after the 5th generation with the exception of the best performer in the 17th generation. The best performer had a normalized $LcTot$ variable of 2.37. It was anticipated that the GA would maximize this parameter since longer conic sections with a given cone radius would result in smaller cone angles, thus resulting in a more stream-line shape. Further work is recommended to investigate the reason for this unexpected result.

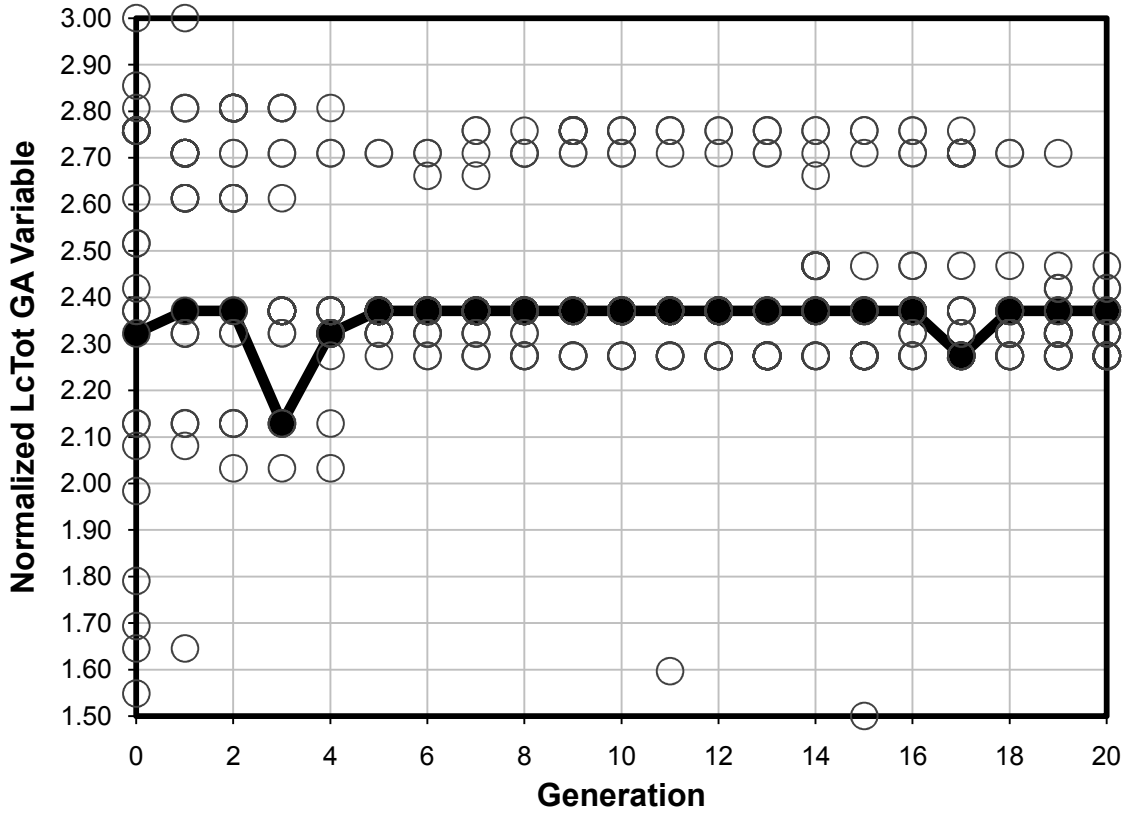


Figure 23: Pressure Fluctuation Study Variable Distribution for LcTot

The variable distribution of the normalized first cone length, $Lc1$, is shown in Figure 24. The variables tend to be distributed throughout the upper half of the design space for the first few generations. By about the 7th generation however, most members have normalized first cone lengths between 0.15 and 0.20. The best performer, however, does not change after the 5th generation. The best performer had a normalized $Lc1$ parameter of 0.176.

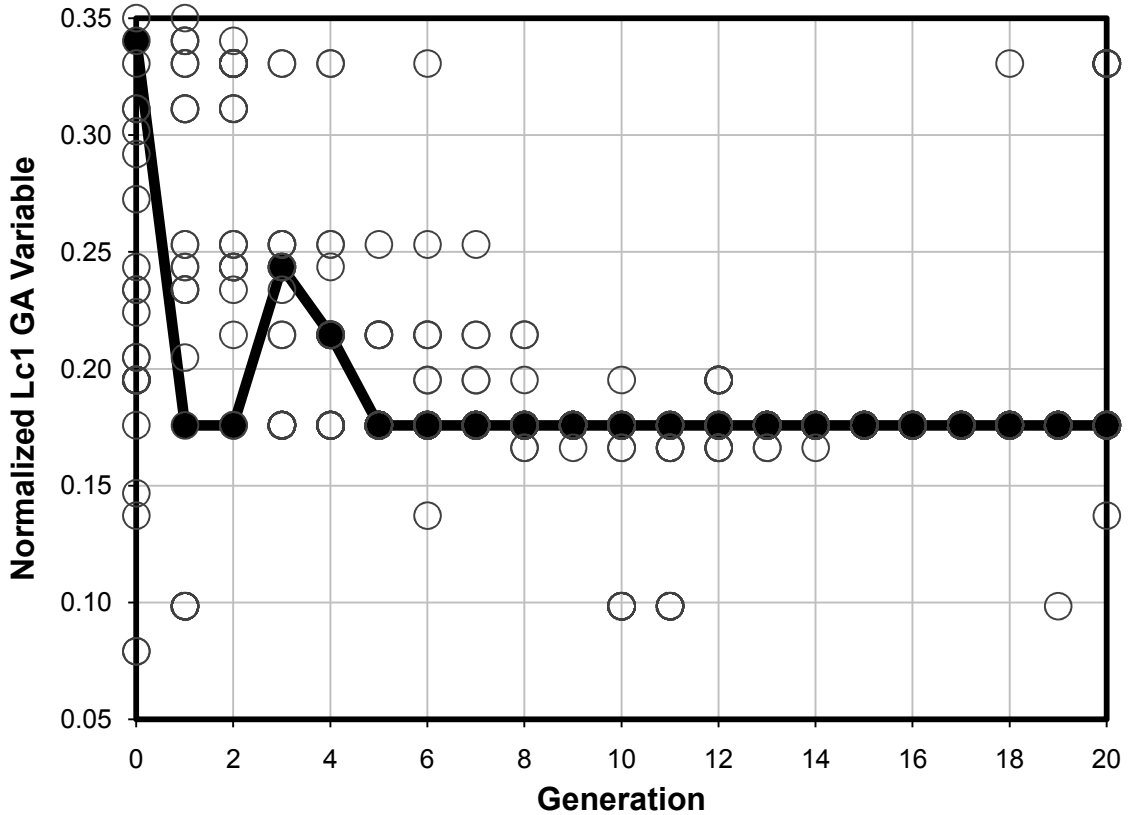


Figure 24: Pressure Fluctuation Study Variable Distribution for Lc1

Shown in Figure 25 is the distribution for the normalized length of the third conic section, $Lc3$. This figure shows a very sparse selection of the $Lc3$ parameter throughout the optimization run. The GA begins to slightly narrow its selection by the 5th generation to the upper region of the design space; however the variable selection is still very spread out compared to the other variable distribution plots. The reason for this could be related to the impact this variable has on the cone angle for the third conic section. The angle of the third conic section has a substantial impact on the flow characteristics at the point where the pressure fluctuation is calculated. By about the 14th generation the selection falls mostly between 0.40 and 0.50, with the best performer of the last generation having a normalized $Lc3$ variable of 0.402.

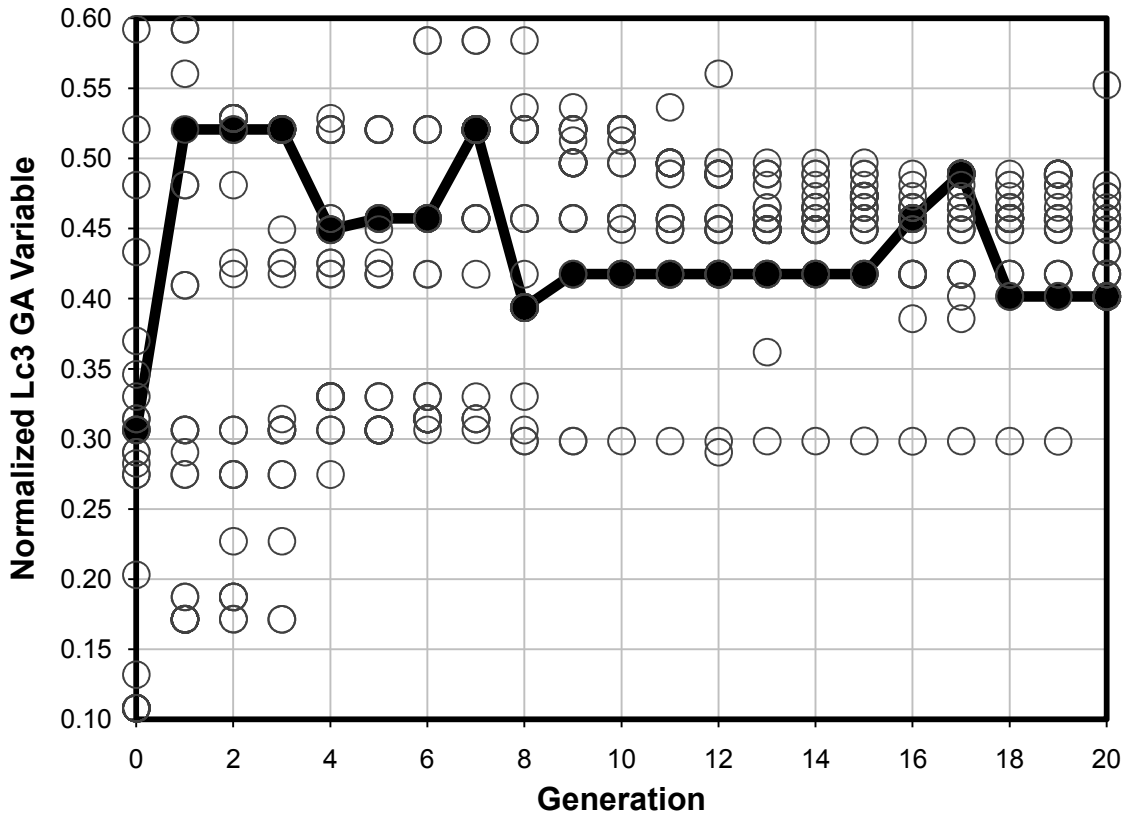


Figure 25: Pressure Fluctuation Study Variable Distribution for Lc3

Shown in Figure 26 is a comparison of the pressure distributions for the baseline and optimized geometries at the Mach 0.85 flight condition, which was the condition where the peak pressure fluctuation level was calculated in this study. This figure shows a clear difference in the pressure distribution throughout the conic sections for the two geometries. In particular, there is a significant difference in the pressure field near the point at which the pressure fluctuation was calculated. The pressure in the region of the flow near this point is substantially higher pressure for the optimized geometry than for the baseline geometry. Note that the pressure scale shown in Figure 26 is gage pressure in pascals, thus 0 is the standard pressure at altitude.

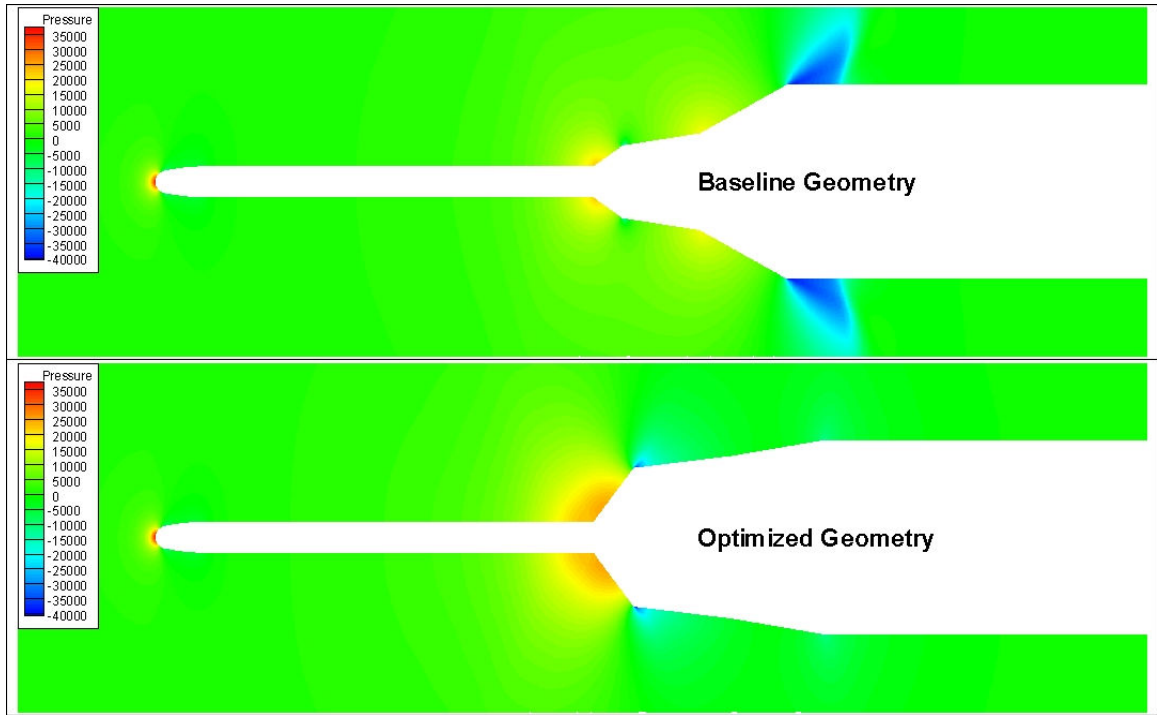


Figure 26: Pressure Fluctuation Study Pressure Distribution Plot for Baseline and Optimized Geometries for Mach 0.85 Flight Condition

A comparison of the dynamic pressure distribution for the baseline and optimized geometries is shown in Figure 27. Since the ascent trajectory used for this study experiences maximum dynamic pressure near the Mach 1.50 flight condition, this is the condition shown in the figure for comparison. This figure shows a moderate difference in the dynamic pressure field near the point at which the pressure fluctuation level is calculated. The most significant difference in the dynamic pressure occurs near the first conic section. The dynamic pressure is so low due to the low flow velocity in this region.

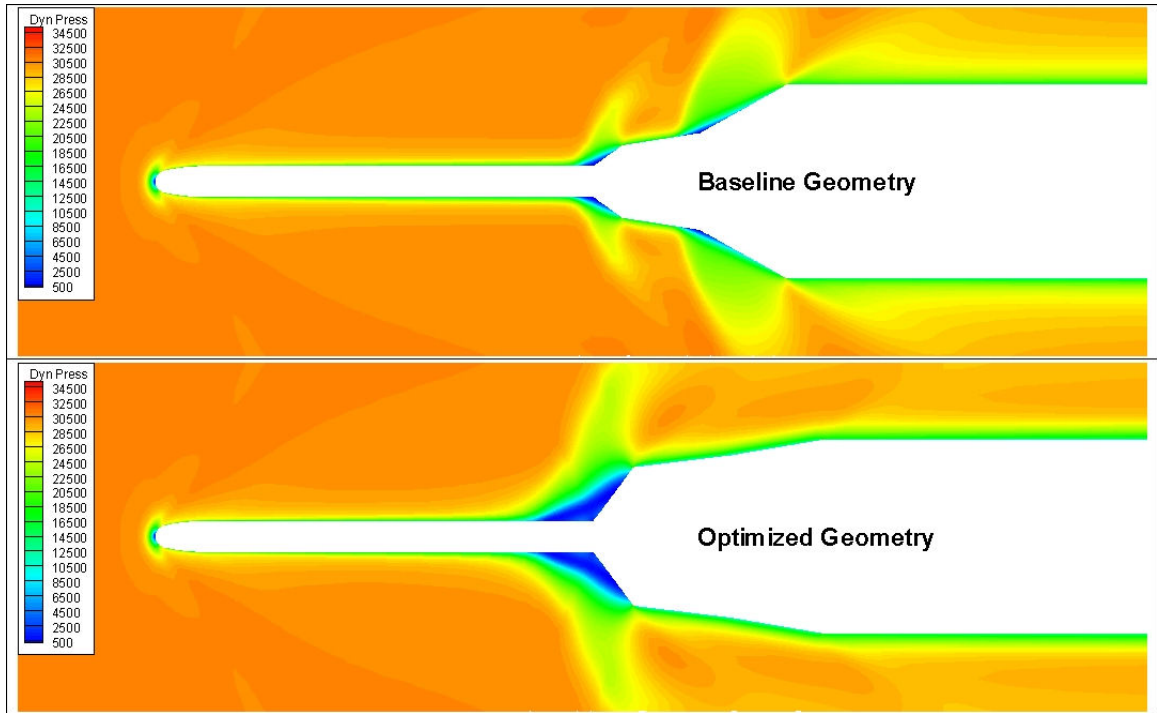


Figure 27: Pressure Fluctuation Study Dynamic Pressure Distribution Plot for Baseline and Optimized Geometries for Mach 1.50 Flight Condition

To further show differences in the flow field for the baseline and optimized geometries, the distribution of the x component of velocity is shown in Figure 28. This figure shows a field plot of the axial velocity component for the Mach 0.85 flight condition. This figure shows a significant difference in the velocity distribution near the conic sections for both geometries. The most important difference of interest in this study is the substantial reduction in the flow velocities for the optimized geometry near the point aft of the third conic section. This reduction in flow velocity near this point is the result of the GA's selection of geometric parameters. Since the third cone angle of the optimized geometry is small compared to that of the baseline geometry the flow is not accelerated as much as it passes over the corner.

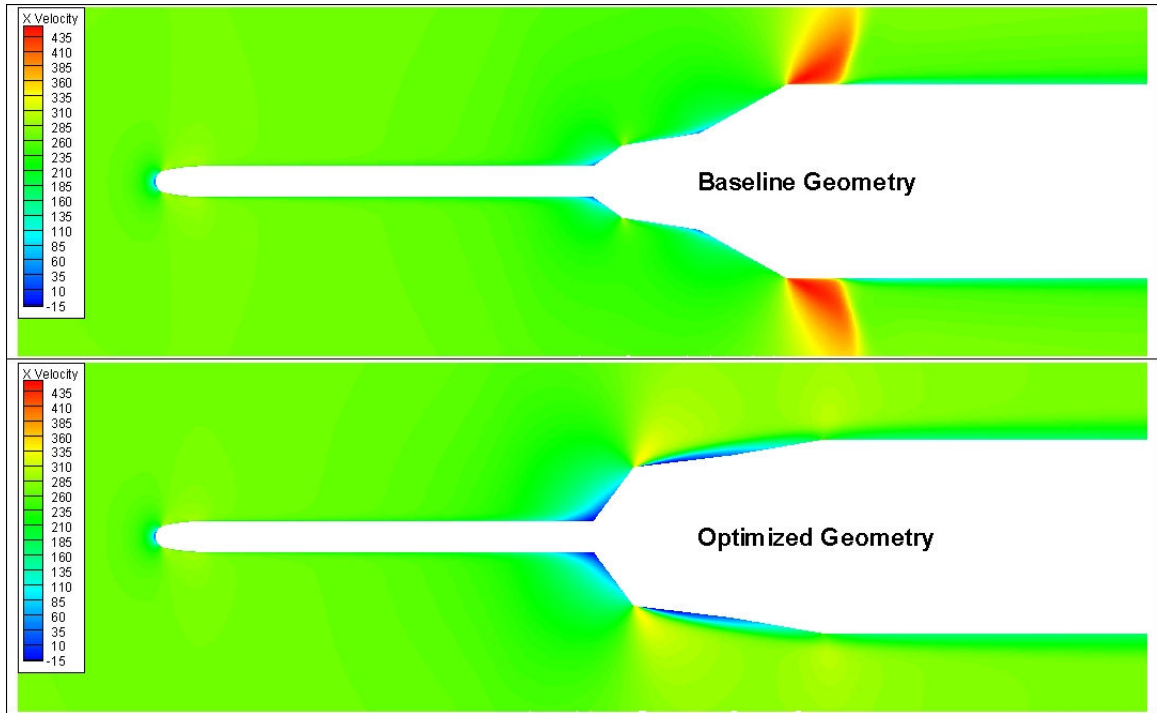


Figure 28: Pressure Fluctuation Study Velocity Distribution Plot Comparison at Mach 0.85 Flight Condition

To show more detail in the x velocity distributions for the baseline and optimized geometries, a close-up of the flow velocity near the conic sections at the Mach 0.85 flight condition is shown in Figure 29 including streamlines. This figure again shows the substantial decrease in flow velocity near the point where the pressure fluctuation is calculated. This figure also shows more clearly the new problematic area aft of the first conic section that arises in the optimized geometry. Figure 29 shows that a separated region of flow develops aft of the first conic section. It is suspected that this would result in higher fluctuating pressure levels at this point than at a similar point for the baseline geometry, thus making the optimized geometry not ideal as a practical design for a launch vehicle. As mentioned previously however, the objective of this study is to

demonstrate a methodology for reducing the pressure fluctuation level, which has been accomplished by the presented results.

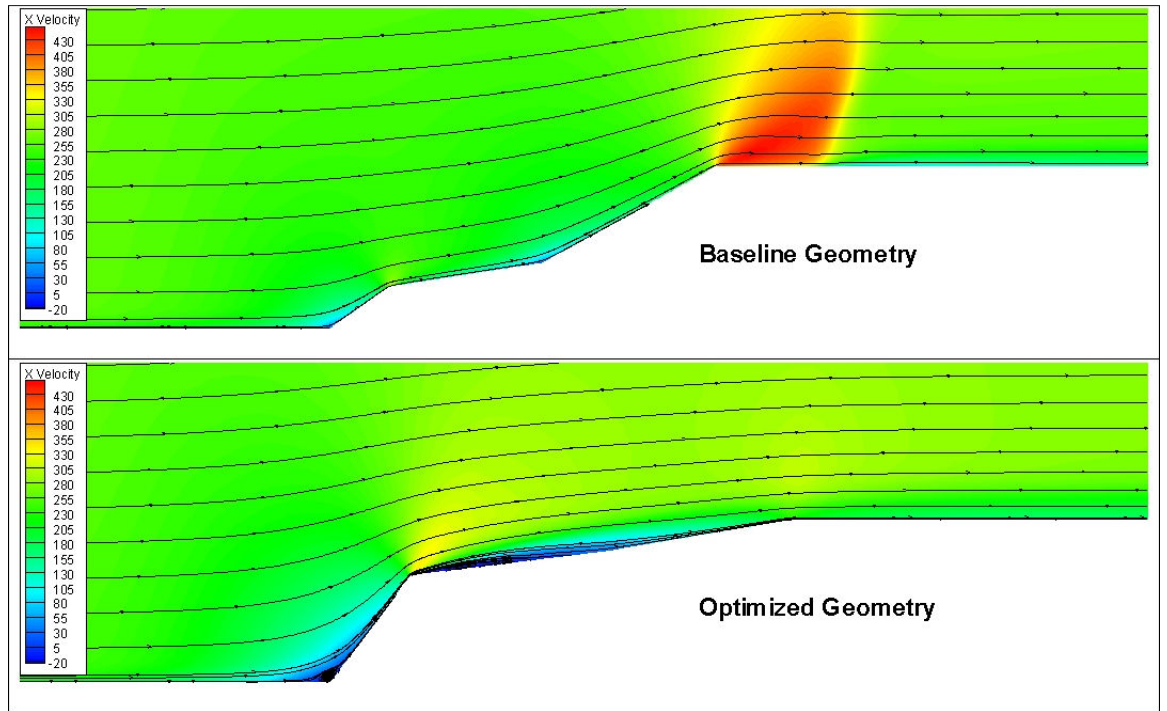


Figure 29: Velocity Distribution Close-Up for Baseline and Optimized Geometries for Pressure Fluctuation Study at Mach 0.85

3.3 AXIAL FORCE MINIMIZATION STUDY

3.3.1 CONVERGENCE CRITERIA

Since the axial force coefficient is the parameter of interest for this study, it is desirable to monitor CFD solution convergence based on the axial force coefficient. Fluent does have the option of calculating the axial force coefficient, however Fluent is not able to monitor solution convergence based on the axial force coefficient. As with the pressure fluctuation study, it was necessary to investigate at what point the residuals for continuity, x -momentum, y -momentum, energy, k , and ε were at when the axial force

coefficient was sufficiently converged. The course grid and Mach 0.85 flight condition was used for determining the convergence criteria for the same reason as discussed previously for the pressure fluctuation study.

This Mach 0.85 flight condition was run for 15000 iterations to allow for plenty of time for the CFD solver to obtain a converged solution. Figure 30 shows the residuals and axial force coefficient plotted against the number of iterations. This figure shows that the residuals have completely converged around 6000 to 7000 iterations. The axial force coefficient, however, converged much sooner at less than 2000 iterations. At 2000 iterations all the residuals had converged to 10^{-6} or lower, except for the continuity residual, which had converged to approximately 10^{-5} . To ensure adequate convergence of the axial force coefficient, the solution was deemed converged once all the residuals reached 10^{-6} within a maximum of 10000 iterations. If a particular member did not meet this convergence criterion then that member was disqualified by setting the axial force coefficient to an extremely high value of 1000. This disqualification is similar to that discussed in section 3.2.1 for the pressure fluctuation study.

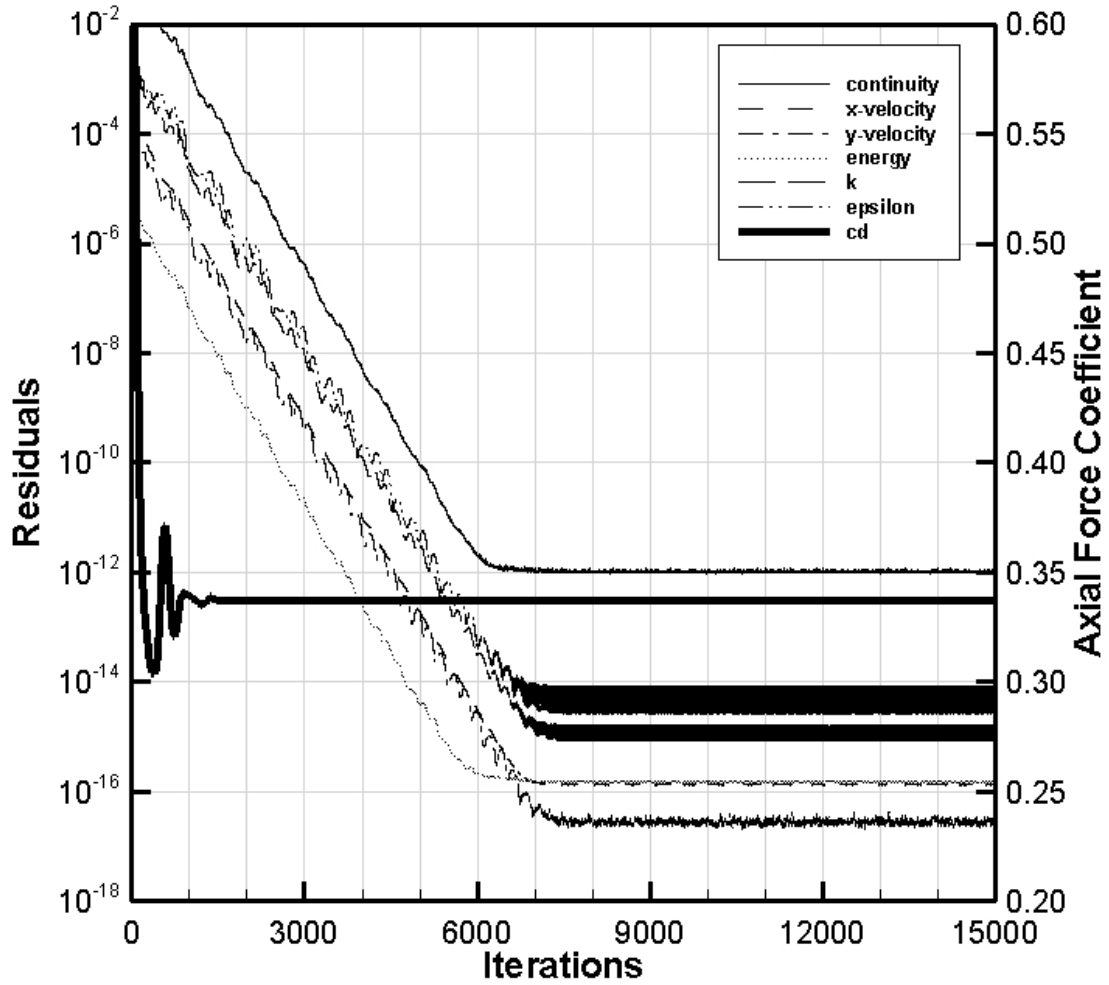


Figure 30: Residuals and Axial Force Coefficient Convergence for the Course Mesh and Mach 0.85 Flight Condition

As with the pressure fluctuation study, it was realized that this convergence criteria was not sufficient for all the possible geometries allowed in the prescribed design space. For some members at certain flight conditions, the residual for continuity would converge to a value less than 10^{-6} thereby never actually meeting the convergence criteria. The axial force coefficient was found to be sufficiently converged for these cases however. To prevent the possibility of the GA eliminating these members which may have good performance, an additional convergence criterion was implemented similar to that of the

pressure fluctuation study. This criterion was a check to see if the axial force coefficient had converged even if the residual convergence criterion was not satisfied. The axial force coefficient was deemed converged if the value was found to not differ by more than 0.1% over the final 2000 iterations. If the member failed this axial force convergence criterion, then the member was disqualified by setting the axial force coefficient to a high value as mentioned previously.

3.3.2 AXIAL FORCE MINIMIZATION RESULTS

As shown in Figure 7 the average axial force coefficient throughout the prescribed ascent trajectory for the baseline geometry is approximately 0.467. For comparison, the V-2 missile at zero angle of attack has an average axial force coefficient of about 0.26. This value was obtained from an axial force coefficient versus Mach number plot for the V-2 missile in Sutton.⁴² The axial force coefficient varies as a function of flight Mach number and this is shown for the baseline geometry in Figure 8. The average axial force coefficient for the optimized geometry is approximately 0.204. This was a reduction of about 56% from the baseline geometry. The GA arrived at this optimized solution after 20 generations.

Figure 31 shows the axial force coefficient throughout the prescribed ascent trajectory for the baseline and optimized geometry. The figure shows that the axial force profile during ascent follows approximately the same trend for both geometries where the axial force profile for the optimized geometry is substantially lower. Also, there is not as much of a change in axial force from the lowest point at Mach 0.5 to the peak at Mach 1.5. The baseline geometry peak axial force at Mach 1.5 is about 5 times that of the Mach

0.5 condition, while the optimized peak axial force at Mach 1.5 is about 4.5 times the Mach 0.5 flight condition. The important result of Figure 31, however, is the substantial decrease in the axial force coefficient for all five points in the ascent trajectory. For most flight conditions the axial force coefficient is reduced by about 50%. The largest axial force reduction was achieved for the Mach 0.85 flight condition, in which a 70% reduction in the axial force coefficient was achieved.

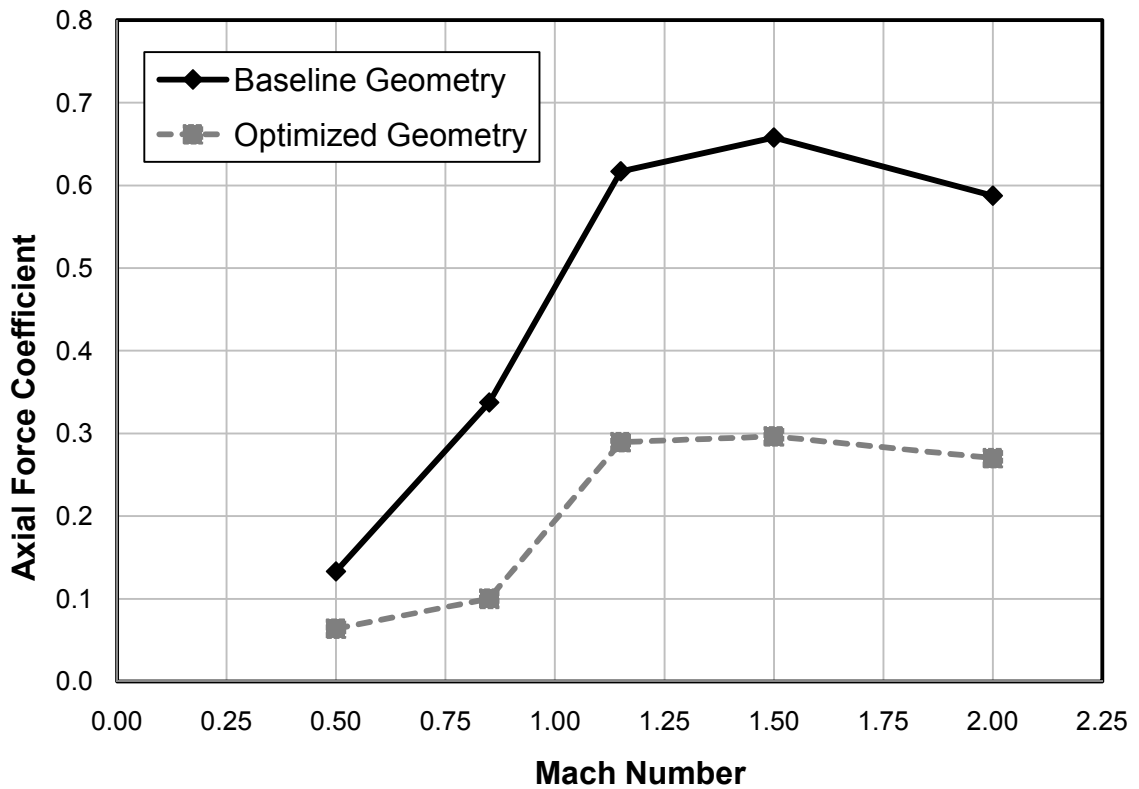


Figure 31: Axial Force Coefficient throughout Ascent for Baseline and Optimized Geometries

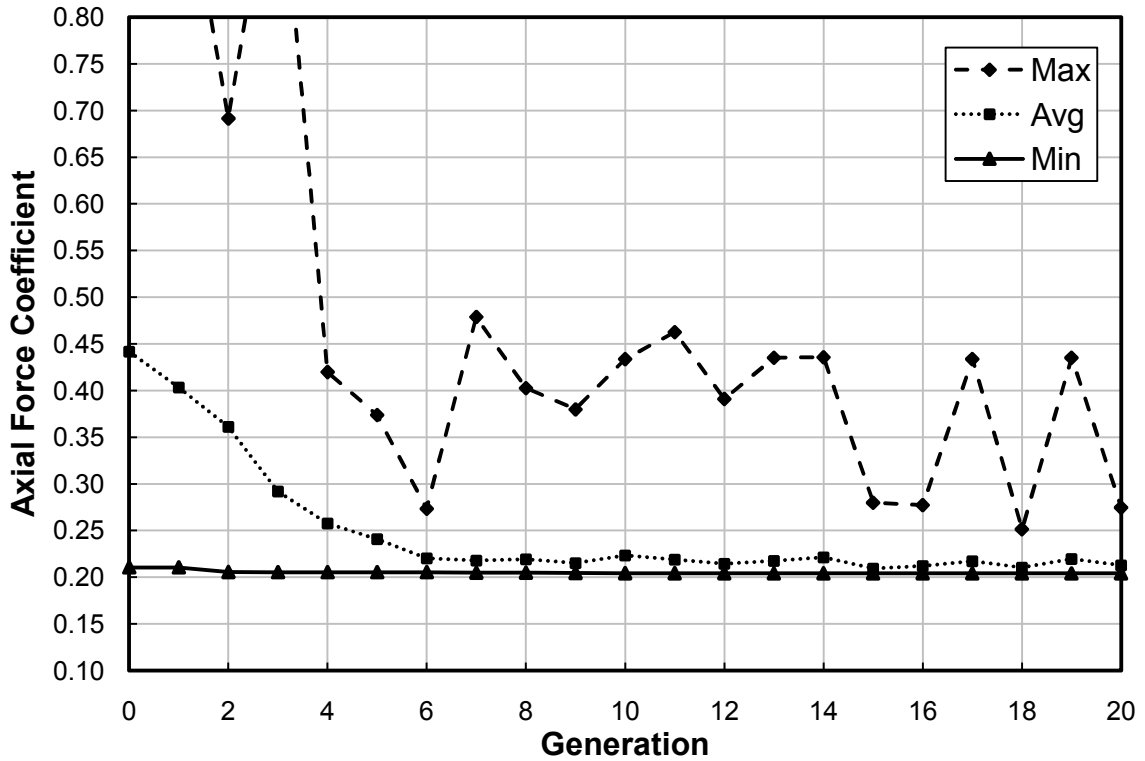


Figure 32: Maximum Average and Minimum Axial Force Coefficient Evolution

The evolution of the axial force coefficient throughout the total number of generations allowed for this study is shown in Figure 32 and Figure 33. Figure 32 shows how the maximum, average, and minimum axial force coefficient members change for each generation. The erratic behavior of the maximum axial force members is expected due to the GA’s random manipulation of some members. It is also important to note in Figure 32 that the maximum axial force coefficient members in the initial, first, and third generations are off the graph. This is because these generations generated members that were disqualified in which the axial force coefficient was set to 1000. Further examination showed that these members were disqualified due to a “bad geometry” as discussed in section 3.1. There were a total of five members that were disqualified, three

of which were in the initial generation. All five of these disqualifications were due to geometry issues. No member was disqualified due to solution convergence.

Another notable result shown in Figure 32 is the small change in the best performer throughout the generations. The best performer is shown by itself in Figure 33 in which the details of how it changes through the generations can be more clearly seen. The GA was able to reduce the axial force coefficient by only 3% from the first to the last generation. This result indicates that the GA was able to come close to the optimized geometry in the initial generation by the random selection of members within the design space. Shown in Figure 32, the plot of the average member for each generation shows that the GA was able to quickly learn what combination of parameters produced good performers. By the sixth generation the average member performed nearly as well as the best performer.

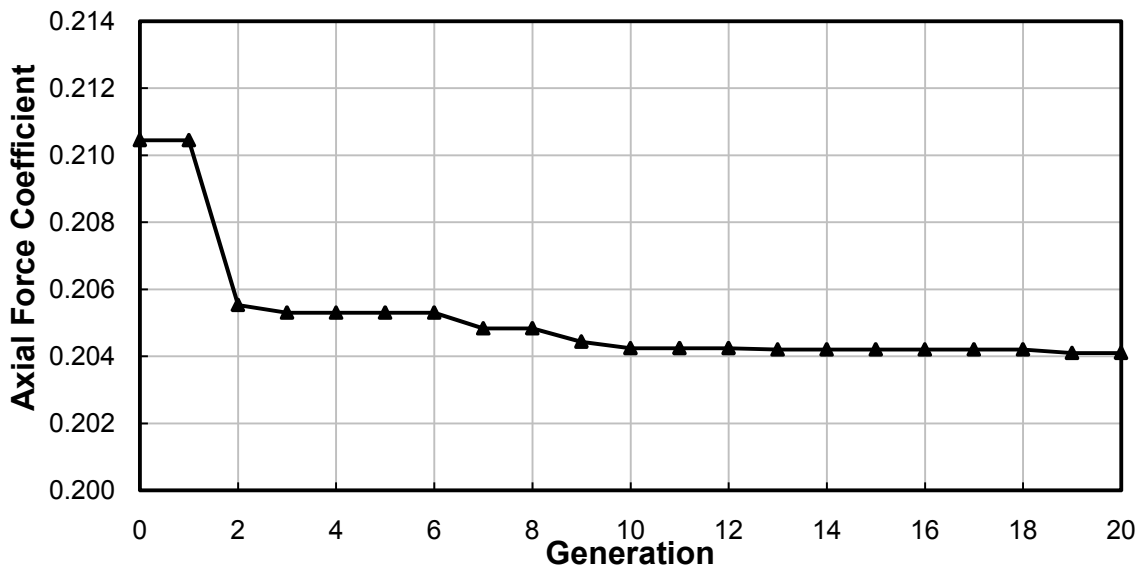


Figure 33: Minimum Axial Force Coefficient Evolution

Table 5 shows the optimized geometric parameters and the minimum and maximum values allowed for each parameter. The only parameter that was maximized by

the GA was the overall length of the conic sections, $LcTot$. All other parameters fell within the prescribed design space. This result indicates that the solution obtained from the GA is a near optimal geometry to minimize axial force. It is plausible that further reduction in axial force could be obtained by allowing the overall length to increase. However, as indicated by the change of the best performer over the generations as shown in Figure 32 and Figure 33, it is not expected that a significant reduction in axial force would occur. Also, while increasing the overall length might reduce axial force, it becomes impractical to design longer and longer conic sections.

Table 5: Optimized Parameters and Design Space

<i>Parameter</i>	<i>Minimum</i>	<i>Maximum</i>	<i>Optimized</i>
Rc1	0.50	1.00	0.629
Rc2	0.40	0.99	0.857
LcTot	1.50	3.00	3.000
Lc1	0.05	0.35	0.302
Lc3	0.10	0.60	0.283

To clearly show how the optimized geometry differs from the baseline geometry, a comparison of the geometries is shown in Figure 34. It was interesting to notice that the optimized geometry consists of conic sections that have a more parabolic or blunted ogive shape. This result was expected as the blunted ogive shape is a commonly used geometric shape in aerodynamics since it has very good aerodynamic performance.

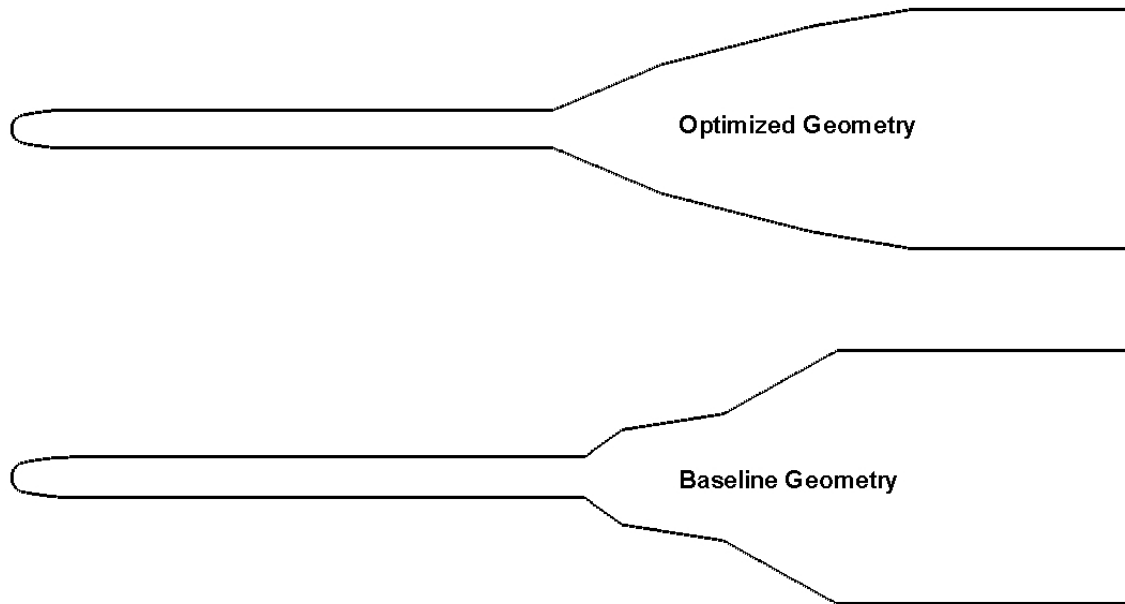


Figure 34: Best Performer and Baseline Geometry Comparison

Figure 35 shows the distribution of first cone radius, $Rc1$, by generation. Initially the members are distributed somewhat uniformly throughout the design space due to the random selection by the GA. By the sixth generation it is clear that the GA has narrowed the selection of the $Rc1$ radius to between 75% and 63% of $Rc2$. By the 15th generation, the GA had further narrowed the radius to between 67% and 63% with the exception of the one outlier in the 19th generation. This outlier is the result of the mutation procedure the GA conducts to include randomness in the member generation process. The optimized geometry had an $Rc1$ variable of 62.9% of the second cone radius, $Rc2$.

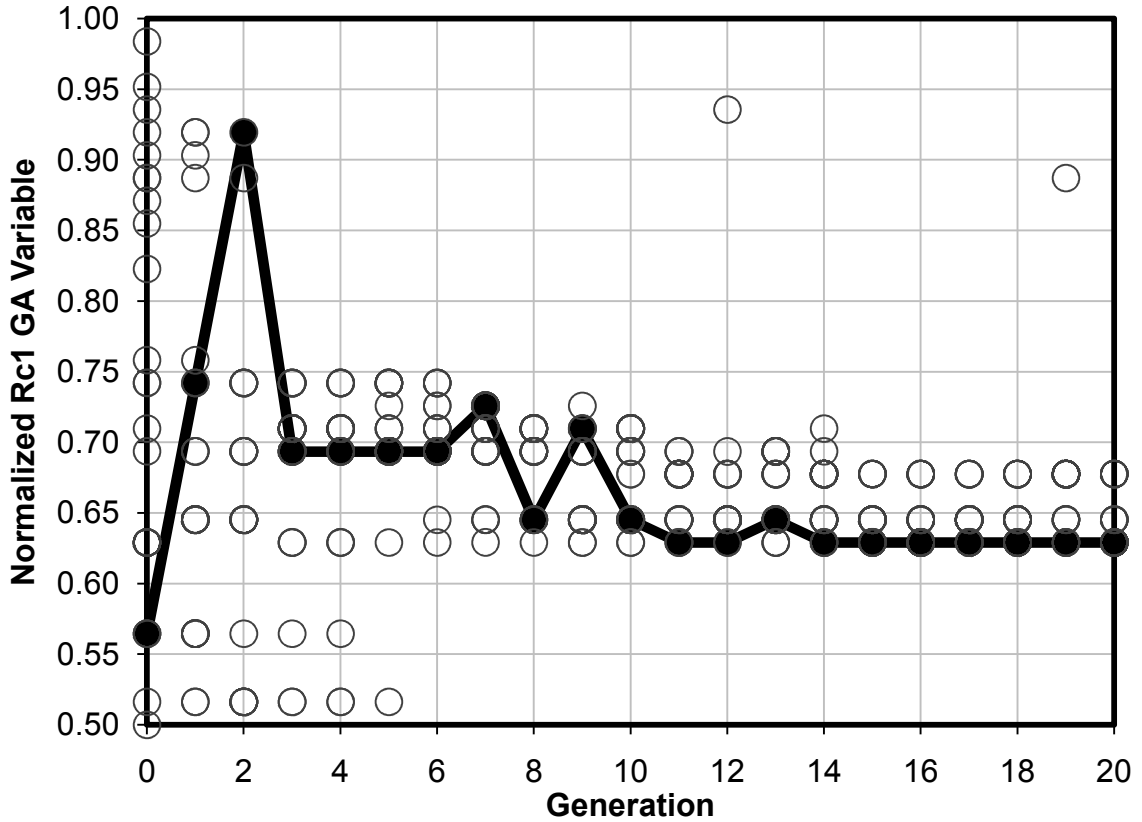


Figure 35: Axial Force Study Variable Distribution for Rc1

The distribution of the second conic section radius, $Rc2$, is shown in Figure 36. As with the $Rc1$ variable, the members are distributed somewhat uniformly throughout the design space initially. By the sixth generation the GA had significantly narrowed down the range to between 85% and 90% of the base radius, Rb . The majority of members continue to fall in this range for the remainder of the optimization run with the exception of the outliers in generations 10,12,13,15, and 17. The $Rc2$ variable was 85.7% of the base radius for the optimized geometry.

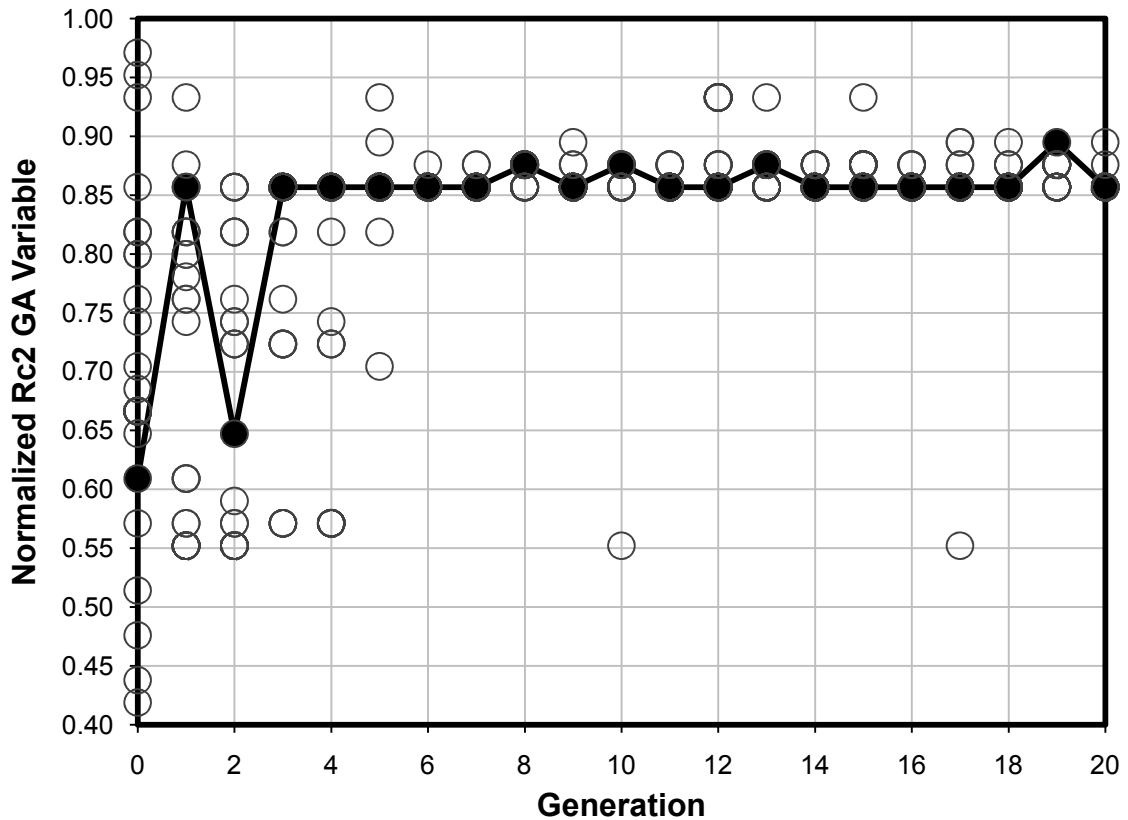


Figure 36: Axial Force Study Variable Distribution for Rc2

The total length of the conic section, $LcTot$, variable distribution by generation is shown in Figure 37. This figure clearly shows the tendency for the GA to generation members that maximized the total length of the conic sections. With the exception of the few outlying members in generations 15, 16, 17, and 20, most all the members after the 6th generation had a total conic section length at the upper limit of the design space. This result was no surprise as the effects of pressure were expected to be much more important than viscous effects on the axial force coefficient. This indeed turned out to be the case for the optimized design. The optimized geometry had a total length of the conic sections of 300% of the base radius, Rb .

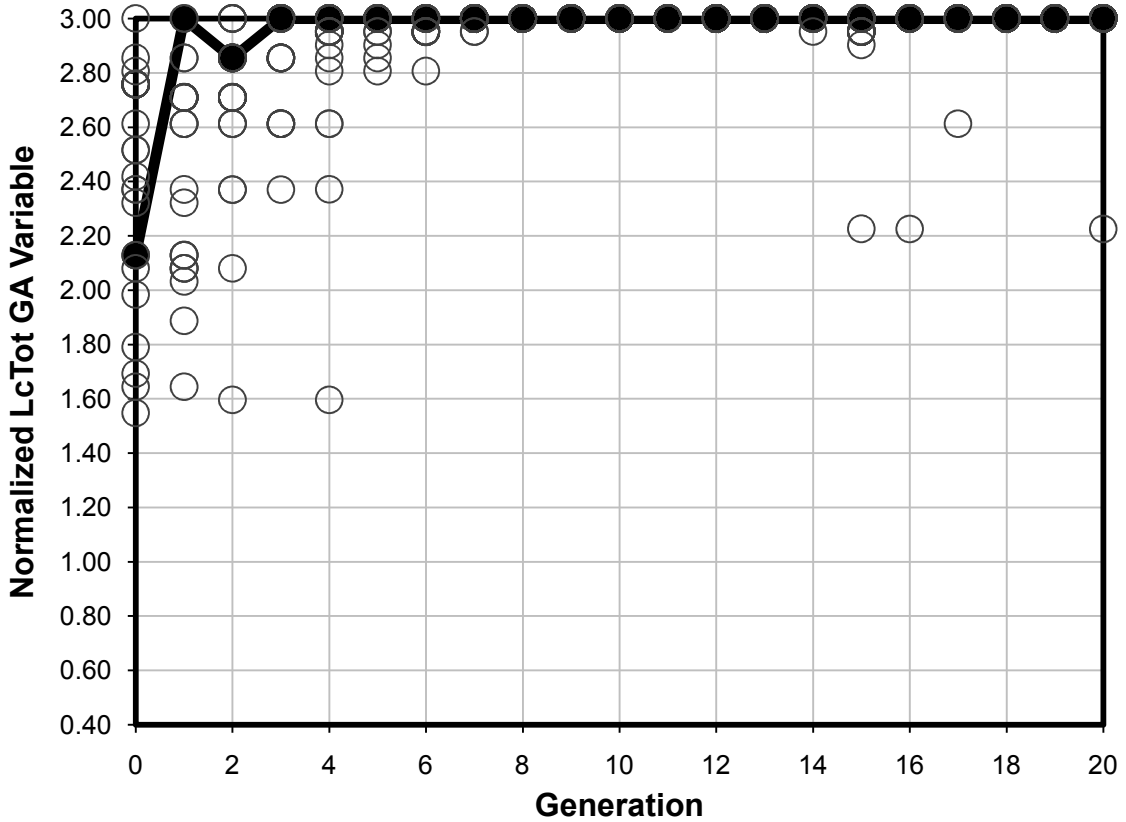


Figure 37: Axial Force Study Variable Distribution for LcTot

Figure 38 shows the variable distribution of the first cone length, $Lc1$. As with the total length of the conic sections, the GA produces members that mostly have a first cone length at the upper limit of the design space. In the 7th generation the GA only generated members that had first cone lengths of 34% to 35% of the total length of the conic sections. This indicates that the optimized geometry would have the longest allowable first cone length. However, after the 7th generation the distribution becomes more spread out, increasing the range to about 30% to 35%. This happened because the best performer for the 8th generation had an $Lc1$ slightly less than the maximum allowed, whereas the best performers for several generations prior had a maximum $Lc1$. The GA continued to generate best performers with smaller first cone lengths, so the GA diversified the

selection of this parameter. The optimized geometry had a first cone length of 30.2% of the total length of the conic sections.

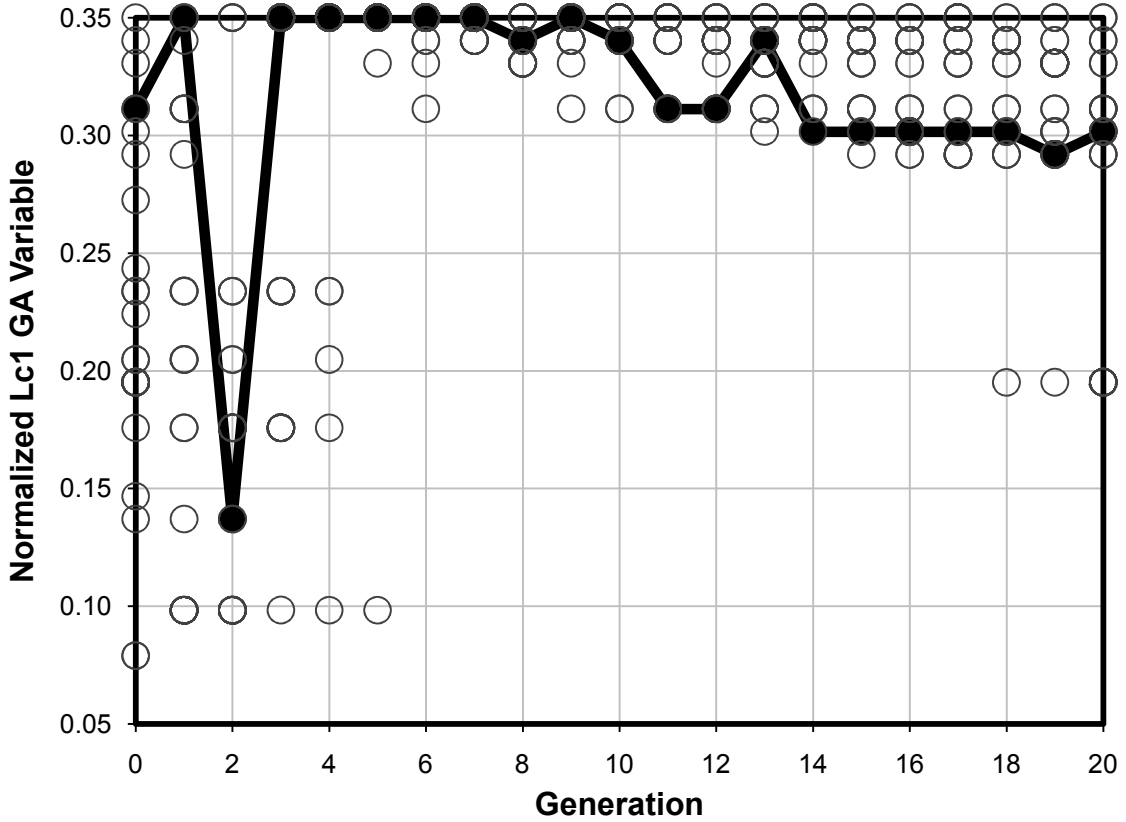


Figure 38: Axial Force Study Variable Distribution for Lc1

The distribution of the third cone length, $Lc3$, is shown in Figure 39. As with the rest of the parameters the initial distribution of the $Lc3$ variable is fairly uniformly distributed throughout the prescribed design space. Also similar to the other parameters, the GA quickly narrows the selection of the third cone length by about the 6th generation. From the 7th generation on the majority of members have a third cone length of between 25% and 30% of the total length of the conic sections. The optimized geometry had a cone length of 28.3% of the total length of the conic sections.

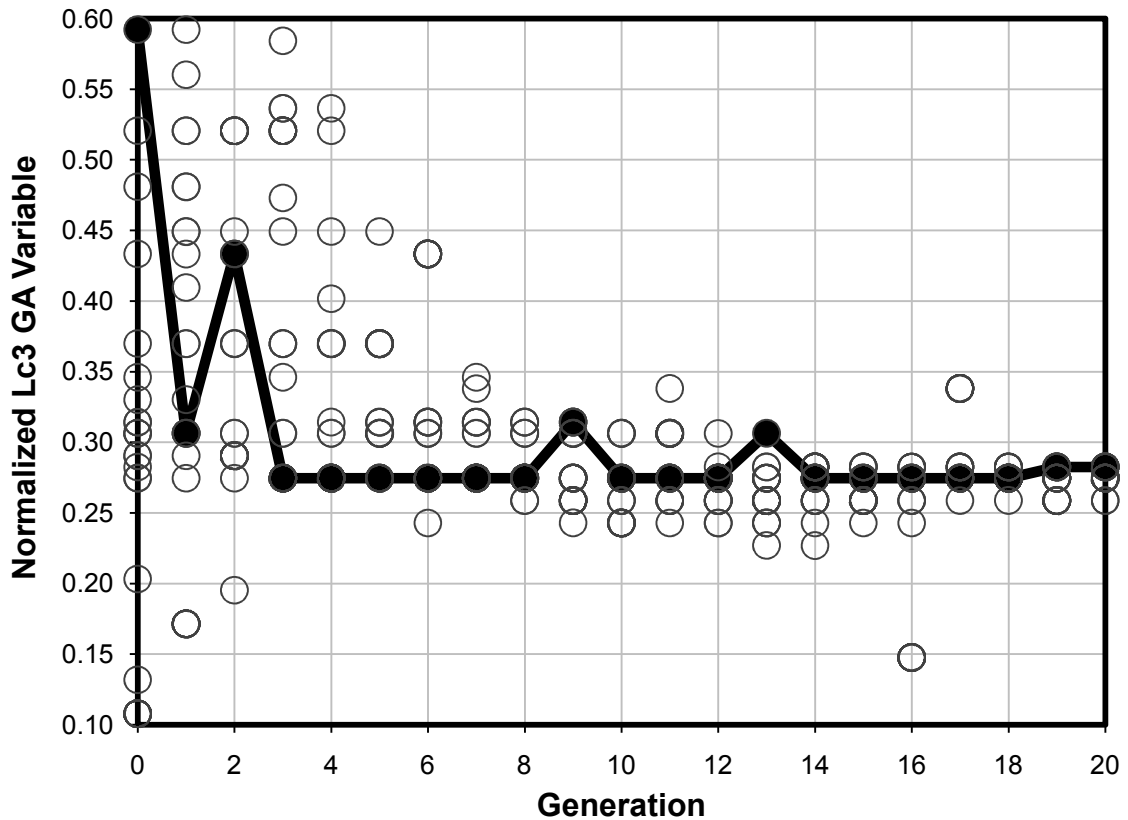


Figure 39: Axial Force Study Variable Distribution for Lc3

Figure 35 through Figure 39 show the distribution of the normalized GA parameters throughout the optimization run. The results shown in these figures indicate that the total length of the conic sections plays an important role in the minimization of the axial force coefficient. Since the GA maximized $LcTot$, this is another indication that pressure is more important to the total axial force than viscous effects, as expected for this geometry and flight conditions. Another feature of the geometry that plays an important role in minimizing axial force is the angle for each conic section, which is dependent upon the radius and length of each conic section. It is evident from the results of this study that an optimal shape for minimizing axial force would be as long as possible while having a parabolic or blunted ogive-type shape.

The parabolic or blunted ogive shape the GA generated was expected to be the optimized geometry since similar shapes have shown to have good aerodynamic characteristics for generating low axial force. The optimization study produced a shape that is very similar to a blunted ogive in that the first conic section is relatively short with a larger angle compared to the second and third conic sections. The other conic sections are much longer with smaller cone angles producing the blunted ogive-like shape. This shape serves to give good aerodynamic characteristics by having little flow separation through the conic sections. While the cone angles became smaller in each conic section it was not expected that the third conic section would have a shorter length than the second conic section.

A pressure distribution plot of the flow field for both the baseline and optimized geometry is shown in Figure 40. Again, it is important to note that the pressure values indicated in this figure are relative to the freestream static pressure, thus 0 pressure is the ambient static pressure. Considering just the conic sections, the pressures are much higher for the baseline geometry than for the optimized geometry. The significant reduction in pressure near this region of the optimized geometry is the primary reason for the large reduction in axial force on the vehicle.

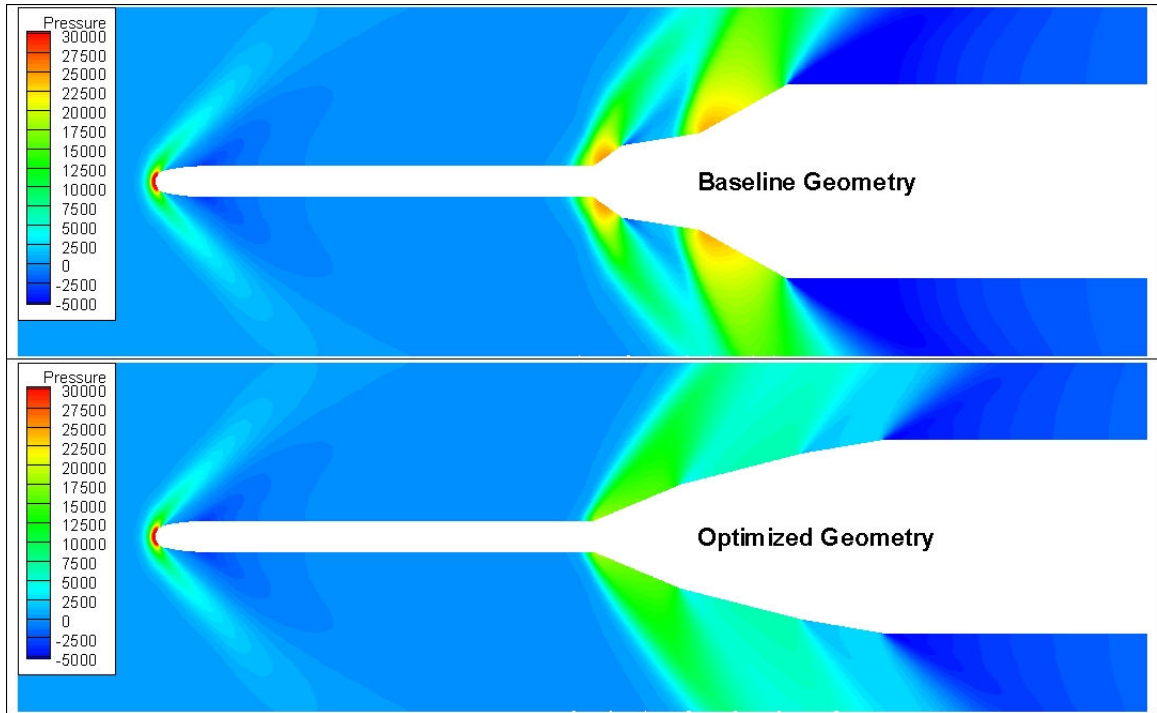


Figure 40: Axial Force Study Pressure Distribution for Baseline and Optimized Geometries at Mach 1.50 Flight Condition

The results of the axial force minimization study have shown a significant reduction in the vehicle's axial force coefficient with a modification of the geometry of the conic sections. A key geometric parameter of the section that had a great impact on the axial force coefficient was the total length of the conic sections, L_{cTot} . Since the GA maximized this parameter, it can be assumed that perhaps further extending the design space for this parameter would result in a further reduction of the axial force coefficient. However, the longer the conic sections become, the more impractical the vehicle design becomes. Longer sections would ultimately result in a heavier vehicle, which would reduce the amount of payload the vehicle would be able to launch to orbit. So there is a tradeoff that must be done in order to determine how much reduction in axial force can be obtained while not adding too much weight, such that the amount of payload-to-orbit is

increased. Since this thesis is set out to demonstrate a method for reducing axial force, determining this tradeoff is beyond the scope of this study; however further work regarding this topic is encouraged.

4 CONCLUSIONS AND RECOMMENDATIONS

An axisymmetric CFD model has been combined with a GA to optimize the geometric shape of a launch vehicle. This vehicle shape was optimized to minimize both the pressure fluctuation level at a critical point and the axial force coefficient. This model was meshed with a structured grid using a custom written FORTRAN routine to develop the mesh based on the GA selected variables that define the geometry. Measures were taken to ensure that no grid overlap would occur while appropriately distributing nodal points. A grid refinement study was performed to ensure sufficiently accurate results. This refinement study showed that the course grid effectively computed the aerodynamic parameters in a reasonable amount of time. This grid was used by the CFD solver in combination with a GA for both axial force and pressure fluctuation minimization studies.

Further work was conducted to determine the convergence criteria for each optimization study. For the axial force minimization study, this consisted of determining the appropriate residual values for which the axial force coefficient was sufficiently converged. Similarly, the pressure fluctuation study convergence criterion was developed by determining the residual values for which the local pressure was sufficiently converged. Upon trial runs for both studies, it was found that a residual based convergence criterion was not sufficient for the entire design space. An additional

convergence criterion was implemented to determine solution convergence based on the local pressure or the axial force coefficient for the respective optimization studies.

The fluctuating pressure level minimization study showed that the average RMS pressure fluctuation level was reduced by about 17.5% over the five flight conditions investigated. The optimized geometry for the fluctuating pressure level study resembled the shape of a blunted ogive, however with the large first cone angle, it is apparent that such a design would not perform desirably aerodynamically. The goal of this study however, was to demonstrate a methodology for using a GA combined with a CFD solver to minimize pressure fluctuations at a critical point. This goal was achieved by the clear reduction in pressure fluctuations at the point on the geometry investigated in this study.

The axial force minimization study also showed a reduction in axial force from the baseline geometry. The optimized geometry had an average axial force coefficient that was approximately 56% lower than the baseline geometry through the ascent trajectory using a simple axisymmetric CFD model. The GA was able to accomplish this by generating a geometry resembling the shape of a blunted ogive, which has historically given desirable aerodynamic characteristics. While the optimized geometry in the axial force minimization study significantly reduced axial force, it is not entirely clear whether or not this design would be practical. The significant increase in total length of the conic sections could result in additional weight, partially negating the benefits of reduced axial force. Nevertheless, a method for reducing the axial force coefficient of a launch vehicle through a typical ascent trajectory has clearly been demonstrated.

This work is considered to be the first step toward a much more comprehensive aerodynamic optimization for launch vehicles and missiles. In light of the results of this

study, further work is strongly recommended. Concerning the pressure fluctuation study, it is suggested that additional research be carried out to develop more robust methods for minimized pressure fluctuations at several points along the geometry. This could be conducted in a very similar manner to the method discussed in this study. The additional work would mostly include modifications to the objective function such that flow parameters at multiple points are monitored by the CFD solver. Perhaps another investigation of the pressure fluctuation study would be an additional optimization of the geometry that only monitors the flight condition at which the peak pressure fluctuation occurs. This would be a relatively simple modification of the presented work such that only the Mach 0.85 flight condition is included in the CFD batch file. Also, increasing the number of conic sections or representing the expansion section with a curved line such as a third order polynomial would greatly improve the variability of the design space. However, increased flexibility in the geometry would lead to much more complexity in the custom grid generator that was written specifically for this study. A more robust grid generator such as GAMBIT is strongly encouraged for further work using more complex design spaces.

Additional work is also recommended to expand upon the results of the axial force minimization study, particularly concerning the tradeoff between reducing axial force and increasing vehicle weight. Perhaps an optimization study could be carried out in which the goal is maximizing payload instead of minimizing axial force. This of course would involve the addition of various models that could determine vehicle mass as a function of geometric shape among other things. It is also conceivable that both of these optimization studies could be combined as one optimization study that maximizes payload and

minimizes pressure fluctuations during a launch. Such a study would be a much more comprehensive aerodynamic optimization study of a launch vehicle or missile.

REFERENCES

1. Himmelblau, H., Fuller, C. and Scharon, T., "Assessment of Space Vehicle Aeroacoustic Vibration Prediction, Design and Testing," NASA CR-1596, July 1970.
2. Coe, C. F., Chyu, W. J., Dods, J. B., "Pressure Fluctuations underlying attached and Serparated Supersonic Turbulent Boundary Layers and Shock Waves," AIAA Aero-Acoustics Conference, Seattle, WA, Oct 15-17, 1973.
3. Mehta, R. C., "Wall Pressure Fluctuations Over a Bulbous Heat Shield of a Satellite Launch Vehicle," *Acta Mechanica*, Vol. 137, No. 1-2, March 1999, pp. 13-31.
4. Camussi, R., Guj, G., Imperatore, B., Pizzicaroli, A., Perigo, D., "Wall Pressure Fluctuation Induced by Transonic Boundary Layers on a Launch Vehicle," *Aerospace Science and Technology*, Vol. 11, No. 5, June 2007, pp. 349-359.
5. Widhalm, M., "Comparison Between Gradient-Free and Adjoint Optimization of a Flying Wing Transport Aircraft Configuration in the Preliminary-Design," AIAA Paper 2007-4060, 2007.
6. Epstein, B., Jameson, A., Pelgin, S., Roman, D., and Vassberg, J., "Comparative Study of 3D Wing Axial Minimization by Different Optimization Techniques," AIAA Paper 2008-0326, 2008.
7. Obayashi, S., Sasaki, D., Takeguchi, Y., and Hirose, N., "Multiobjective Evolutionary Computation for Supersonic Wing-Shape Optimization," *IEEE Transactions on Evolutionary Computation*, Vol. 4, No. 2, 2000, pp. 182-187.
8. Anderson, M. B., "Using Pareto Genetic Algorithms for Preliminary Subsonic Wing Design," AIAA Paper 96-4023, presented at the 6th AIAA/NASA/USAF Multi-disciplinary Analysis and Optimization Symposium, Bellevue, WA, September 1996.
9. Oyama, A., Obayashi, S., Nakahashi, K., "Transonic Wing Optimization Using Genetic Algorithm," AIAA Paper 97-1854, 13th Computational Fluid Dynamics Conference, June 1997.

10. Shahrokhi, A., Jahangirian, A. "Airfoil Shape Parameterization for Optimum Navier-Stokes Design with Genetic Algorithm," *Aerospace Science and Technology*, Vol. 11, No. 6, 2007, pp. 443-450.
11. Marco, M., Lanteri, S. "A Two-Level Parallelization Strategy for Genetic Algorithms Applied to Optimum Shape Design," *Parallel Computing*, Vol. 26, No. 4, 2000, pp. 377-397.
12. Quagliarella, D., Vicini, A. "Viscous Single and Multicomponent Airfoil Design with Genetic Algorithms," *Finite Elements in Analysis and Design*, Vol. 37, No. 5, 2001, pp. 365-380.
13. Doorly, D. J., Peiro, J., Kuan, T., and Oesterle, J. P., "Optimisation of Airfoils using Parallel Genetic Algorithms," Aeronautics Department, Imperial College, London, UK.
14. Jang, M., and Lee, J., "Genetic Algorithm Based Design of Transonic Airfoils Using Euler Equations," AIAA Paper 2000-1584, Presented at the 41st AIAA/ASME/ASCE/AHS/ASC Structures, Structural Dynamics, and Materials Conference, April 2000.
15. Jones, B. R., Crossley, W. A., and Anastasios, S. L., "Aerodynamic and Aeroacoustic Optimization of Airfoils Via a Parallel Genetic Algorithm," AIAA Paper 98-4811, 7th AIAA/USAF/NASA/ISSMO Symposium on Multidisciplinary Analysis and Optimization, September 1998.
16. Benini, E., and Toffolo, A., "Optimal Design of Horizontal-Axis Wind Turbines Using Blade-Element Theory and Evolutionary Computation," *Journal of Solar Energy Engineering*, Vol. 124, No. 4, 2002, pp. 357-363.
17. Burger, C. and Hartfield, R. J., "Propeller Performance Optimization Using Vortex Lattice Theory and a Genetic Algorithm," AIAA-2006-1067, present at the 44th Aerospace Sciences Meeting and Exhibit, Reno, NV, Jan 9-12, 2006.
18. Anderson, M. B., Burkhalter, J. E., and Jenkins, R. M., "Design of an Air to Air Interceptor Using Genetic Algorithms," AIAA Paper 99-4081, presented at the 1999 AIAA Guidance, Navigation, and Control Conference, Portland, OR, August 1999.
19. Anderson, M. B., Burkhalter, J. E., and Jenkins, R. M., "Intelligent Systems Approach to Designing an Interceptor to Defeat Highly Maneuverable Targets," AIAA Paper 2001-1123, presented at the 39th Aerospace Sciences Meeting and Exhibit, Reno, NV, January 2001.

20. Burkhalter, J. E., Jenkins, R. M., Hartfield, R. J., Anderson, M. B., Sanders, G. A., "Missile Systems Design Optimization Using Genetic Algorithms," AIAA Paper 2002-5173, Classified Missile Systems Conference, Monterey, CA, November 2002.
21. Hartfield, R. J., Jenkins, R. M., Burkhalter, J. E., "Ramjet Powered Missile Design Using a Genetic Algorithm," AIAA 2003-0451, presented at the 42nd AIAA Aerospace Sciences Meeting, Reno, NV, January 5-8, 2004.
22. Jenkins, R. M., Hartfield, R. J., Burkhalter, J. E., "Optimizing a Solid Rocket Motor Boosted Ramjet Powered Missile Using a Genetic Algorithm," AIAA 2005-3507 presented at the 41st AIAA/ASME/SAE/ASEE Joint Propulsion Conference, Tucson, AZ, July 10-13, 2005.
23. Riddle, D. B., "Design Tool Development for Liquid Propellant Missile System," M.S. Thesis, Auburn University, May 10, 2007.
24. Schoonover, P. L., Crossley, W. A., Heister, S. D., "Application of Genetic Algorithm to the Optimization of Hybrid Rockets," AIAA Paper 98-3349, 34th AIAA/ASME/SAE/ASEE Joint Propulsion Conference and Exhibit, July 1998.
25. Nelson, A., Nemec, M., Aftosmis, M., Pulliam, T., "Aerodynamic Optimization of Rocket Control Surfaces Using Cartesian Methods and CAD Geometry," AIAA 2005-4836, 23rd Applied Aerodynamics Conference, Toronto, Canada, June 6-9, 2005.
26. Giro, R., Cyrillo, M., and Galvão, D. S., "Designing Conducting Polymers Using Genetic Algorithms," *Chemical Physics Letters*, Vol. 366, No. 1-2, 25 Nov. 2002, pp. 170-175.
27. Monodoloni, S., "A Genetic Algorithm for Determining Optimal Flight Trajectories," AIAA Paper 96-4023, presented at the 6th AIAA/NASA/USAF Multidisciplinary Analysis and Optimization Symposium, Bellevue, WA, September 1996.
28. Williams, E., Crossley, W., Lang, T. "Average and Maximum Revisit Time Trade Studies for Satellite Constellations Using a Multiobjective Genetic Algorithm," *Journal of the Astronautical Sciences*, Vol. 49, No. 3, 2001, pp.385-400.
29. Karr, C. L., Freeman, L. M., Meredith, D. L., "Genetic Algorithm Based Fuzzy Control of Spacecraft Autonomous Rendezvous," NASA Marshall Space Flight Center, 5th Conference on Artificial Intelligence for Space Applications, 1990.
30. Krishnakumar, K., Goldberg, D. E., "Control System Optimization Using Genetic Algorithms," *Journal of Guidance, Control, and Dynamics*, Vol. 15, No. 3, May-June 1992.

31. Perhinschi, M. G., "A Modified Genetic Algorithm for the Design of Autonomous Helicopter Control System," AIAA-97-3630, Presented at the AIAA Guidance, Navigation, and Control Conference, New Orleans, LA, August 1997.
32. Anderson, M. B., "Design of a Missile Interceptor Using Genetic Algorithms," Ph.D. Dissertation, Auburn University, December 14, 1998.
33. Ahujz, V. and Hosangadi, A. "Design Optimization of Complex Flowfields Using Evolutionary Algorithms and Hybrid Unstructured CFD," AIAA Paper 2005-4984, 2005.
34. Chernyavsky, B., Stepanov, V., Rasheed, K., Blaize, M., and Knight, D. "3-D Hypersonic Inlet Optimization Using a Genetic Algorithm," AIAA Paper 98-3582, 1998.
35. Doyle, J. B., Hartfield, R. J., and Roy, C. J. "Aerodynamic Optimization for Freight Trucks using a Genetic Algorithm and CFD", manuscript submitted to the *AIAA Journal*, March 2008 (see also AIAA Paper 2008-323).
36. Holland, J. H. *Adaptation in Natural and Artificial Systems*, The MIT Press; Reprint edition 1992 (originally published in 1975).
37. Nelson, A., Nemec, M., Aftosmis, M., and Pulliam, T. "Aerodynamic Optimization of Rocket Control Surfaces Using Cartesian Methods and CAD Geometry," AIAA Paper 2005-4836, 2005.
38. Perez, R.E., Chung, J., and Behdinan, K. "Aircraft Conceptual Design Using Genetic Algorithms," AIAA Paper 2000-4938, 2000.
39. Doyle, J. B., Hartfield, R. J., Roy, C. J., "Tractor Trailer Axial Optimization by a Genetic Algorithm with CFD," AIAA Paper 2006-3863, Presented at the 24th AIAA Applied Aerodynamics Conference, San Francisco, CA, June 5-8, 2006.
40. Doyle, J. B., "Aerodynamic Optimization for Freight Trucks Using a Genetic Algorithm and CFD," M.S. Thesis, Auburn University, October 2, 2007.
41. "Saturn V Flight Manual – SA 503," MFCS-MAN-503, November 1, 1968.
42. Sutton, G. P., and Biblarz, O., *Rocket Propulsion Elements*, 7th ed., John Wiley & Sons, Inc., New York, 2001, pp. 108.

APPENDIX A: GA Input File

```
.false. ; micro
.false. ; pareto
.true. ; steady_state
.false. ; maximize
.true. ; elitist
.false. ; creep
.false. ; uniform
.false. ; restart
.true. ; remove_dup
.false. ; destroy_elite2
.false. ; niche
.false. ; phenotype
2531 ; iseed
0.9 ; pcross
0.001 ; pmutation
0.05 ; pcreep
1 ; ngoals
1.0 ; xgls(j)
.0 ; domst
2550 ; convrg_chk
5 ; no_para
'par1', 1.0, 0.5, .02, .false. ; xmax xmin resolution niche_par
'par2', 0.99, 0.4, .02, .false. ; xmax xmin resolution niche_par
'par3', 3.0, 1.5, .05, .false. ; xmax xmin resolution niche_par
'par4', 0.35, 0.05, .01, .false. ; xmax xmin resolution niche_par
'par5', 0.6, 0.1, .01, .false. ; xmax xmin resolution niche_par
1 ; ifreq
30 ; mempops
20 ; maxgen
```